APPLICATION OF SPECTRAL INVERISON TO ENHANCE SEISMIC RESOLUTION IN NAM CON SON BASIN, OFFSHORE VIETNAM

A Thesis

Presented to

the Faculty of the Department of Earth and Atmospheric Sciences

University of Houston

In Partial Fulfillment

of the Requirement for the Degree

Master of Science

By

Vu Ha

December 2014

APPLICATION OF SPECTRAL INVERISON TO ENHANCE SEISMIC RESOLUTION IN NAM CON SON BASIN, OFFSHORE VIETNAM

Vu Ha

APPROVED:

Dr. John P. Castagna, Committee Chairman

Department of Earth and Atmospheric Sciences

Dr. Hua-wei Zhou

Department of Earth and Atmospheric Sciences

Dr. Pete Emmet

Brazos Valley GeoServices, Inc

Dean, College of Natural Sciences and Math

ACKNOWLEDGEMENTS

APPLICATION OF SPECTRAL INVERISON TO ENHANCE SEISMIC RESOLUTION IN NAM CON SON BASIN, OFFSHORE VIETNAM

An Abstract of a Thesis

Presented to

the Faculty of the Department of Earth and Atmospheric Sciences

University of Houston

In Partial Fulfillment

of the Requirement for the Degree

Master of Science

By

Vu Ha

December 2014

Abstract

Applications of spectral inversion on a seismic dataset in Nam Con Son basin, Vietnam, have successfully resolved the wavelet interferences created by complex reflectivity patterns of the inter-bedded sand bodies with thin claystones and coal layers. Bandpass filtering was performed to examine different frequency bands of the inverted data for useable signal and lateral coherence. The desired bandwidth for spectral inversion result was 10-100 Hz, almost twice the original bandwidth of 20-65 Hz. Vertical resolution in the reservoir level was increased from 25 m to 15 m. The additional reflections that have resulted from the enhanced frequency content are found to be highly correlated with well logs with an average coefficient of 0.7. Furthermore wavelet deconvolution was applied to improve vertical resolution to 13 m and succeeded in bringing the seismic reflections closer to the earth reflectivity.

Several apparent discontinuities due to wavelet interferences were revealed as continuous geological features by the inversion process. The tops and bases of particular sandstones with thickness greater than 13 m are now resolved and can be interpreted individually, allowing thickness estimation of the reservoir. The main fault systems that were defined from the original seismic data are consistent with the high-resolution data, while additional small faults, with displacements of about 16 m, have become visible in the central fault block, potentially separating the reservoir sand bodies into smaller units.

Tables of contents

1. INTRODUCTION

1.1 General Background

In the subsurface exploration and production of hydrocarbons, one of the important goals is to recognize the internal stratigraphy, lateral continuity, and connectivity of sedimentary bodies that may serve as reservoirs and seals. The ability to determine these features is strongly dependent on the resolution of seismic data. Vertical seismic resolution is defined as the ability to separate or distinguish between two or more closely-spaced reflections. Widess (1973) defined the theoretical resolution limit as $1/8^{th}$ of the wavelength ($\lambda/8$). The tuning thickness usually occurs at about $\lambda/4$, and in practice, beds below tuning thickness are not readily resolved (Kallweit and Wood, 1982).

The theory of spectral decomposition offers the possibility of imaging geologic features below seismic resolution, for thickness determination (Partyka, et al., 1999), reservoir delineation, and stratigraphic visualization (Marfurt and Kirlin, 2001). Partyka (1999) pointed out the inverse relationship between the notch spacing in the frequency domain and the layer thickness in time domain. Different methods of computing the time-frequency analysis of seismic data include discrete Fourier Transform (DFT), continuous wavelet transform (CWT) and Matching Pursuit Decomposition (MPD). Recently Puryear (2012) proposed an inversion based spectral decomposition method called constrained least-squares spectral analysis (CLSSA), which results in better spectral analysis.

1

Spectral inversion combines the principles of spectral decomposition and seismic inversion to extend the theoretical resolution limit below λ/8, where the seismic amplitude and frequency response is more sensitive to thin-beds (Castagna, 2005; Portniaguine and Castagna, 2005; Chopra et al., 2006; Puryear and Castagna, 2008). Zhang and Castagna (2011) detailed a reflectivity inversion method using basis pursuit of a wedge dictionary representing thin-bed reflectivity patterns.

The complex geology and structure of an oil field in Nam Con Son basin, offshore Vietnam, suggests the need for enhancement of the vertical resolution of the seismic data used to define and delineate this feature. It is not always possible to distinguish between top and base of sand bodies on the conventional PSTM (Pre-stack Time Migration) seismic data, making it difficult to estimate the thickness and distribution of such stratigraphic features in the study area. This thesis focuses on the detailed analysis of high-resolution seismic data that resulted from the application of spectral inversion and wavelet deconvolution to answer the questions of whether or not the high-resolution data are valid and able to reliably improve stratigraphic and structural interpretation.

Analysis of the high-resolution data show that spectral inversion successfully resolved the interference effects that have resulted from the complex reflectivity pattern at the reservoir level. The frequency bandwidth of the original seismic data was significantly broadened, which improved the vertical resolution. The results were verified with synthetic well-ties. With the high-resolution data it was possible to recognize and to map previously unresolved beds, in addition several small-throw faults became visible, improving the interpretation of geological features in this area.

1.2 Research Objectives

The main objectives of this work are listed below:

- The research aimed to analyze the high-frequency seismic data that resulted from spectral decomposition and spectral inversion to validate the added frequency content as compared to the original seismic data.

- The research applied wavelet deconvolution to further improve the resolution and obtain a reflectivity solution closer to the Earth reflectivity.

- The research focused on the interpretation the high-resolution data in order to access and quantify the improvement in resolution for stratigraphic and structural interpretation.

1.3 Dataset

The spectral inversion was run over a small volume of about 25 km^2 of 3D PSTM seismic data within a time window from 1500 to 2500 ms (Figure 1.1). This area surrounds the crest of a prominent structural high. Three wells A, C and D were used for analysis and comparison to the seismic data. All wells had log data including gamma ray (GR), sonic (DT) and density (RHOB), which are necessary for the generation of synthetic well-ties and for wavelet extraction. The seismic and well data was provided by Petrovietnam Exploration & Production Corporation.
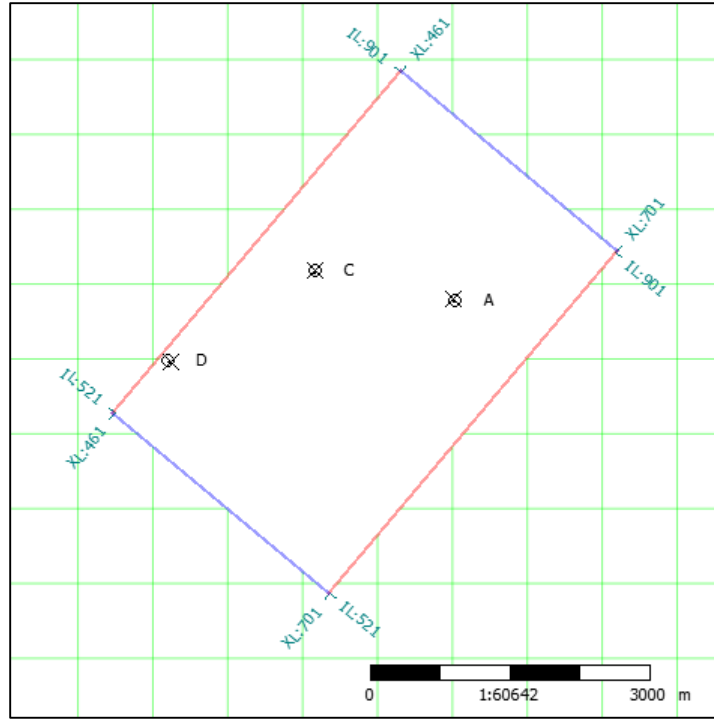
Figure 1.1: Outline of seismic data and well locations

1.4 Method

The original 3D seismic data set was loaded into Hampson Russell and IHS Kingdom

Suite. Well-log editing was performed on the density and sonic logs, such that these logs

were suitable as input for synthetic seismogram generation. All three wells were then tied

to the original seismic data and wavelets were extracted. The spectral inversion was

applied to the data by Lumina Geophysical to obtain a higher frequency seismic data set.

The inverted seismic data was filtered back to a desired bandwidth with good signal to

noise ratio and lateral coherence. Wavelet deconvolution was performed as an extra step

to slightly increase vertical resolution and to obtain a more favorable image for seismic

interpretation. The high-resolution data were quality checked by comparative well-tie

analysis, wavelet extraction and seismic interpretation throughout the volume.
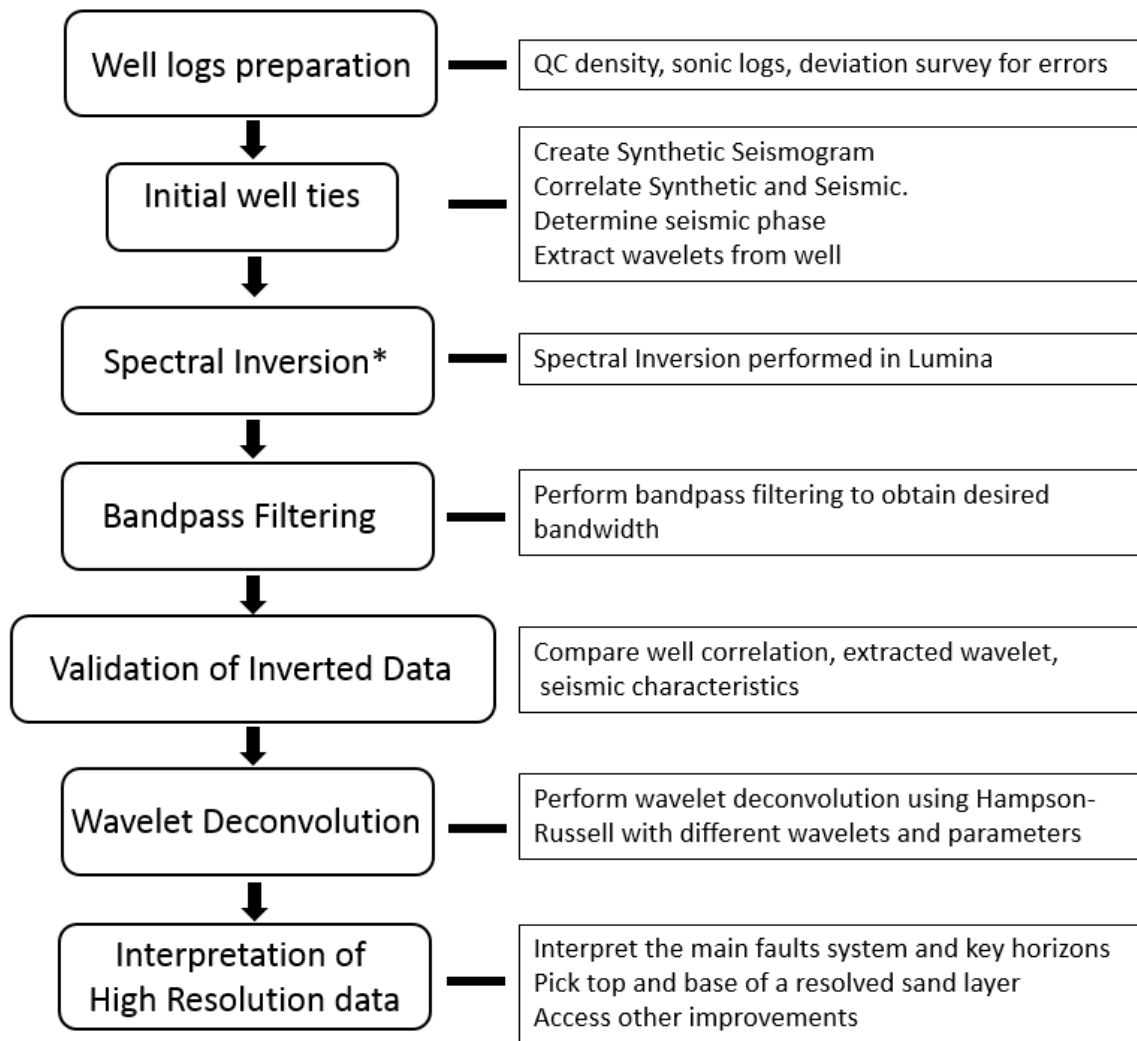
4

Figure 1.2: General workflow

2. GEOLOGICAL BACKGROUND

2.1 Regional Setting

The study area is located in Nam Con Son basin, one of several Tertiary rift basins on the continental shelf, offshore Vietnam. From Paleogene to late Miocene time the basin experienced two main phases of rifting (Matthews et al., 1997). It was initially formed during a Paleogene rifting event caused by the collision of Indian plate against Eurasia. The basin was further developed as a result of extension related to the southwestward propagation of the seafloor spreading in the southwestern sub-basin of the South China Sea (Murray and Dorobek, 2004). The uplift in the southern Vietnam margin ceased the main rifting phase in Nam Con Son basin at the end of Oligocene. The second rifting phase occurred in Miocene and was synchronous with the clastic sediments deposited in inner to outer shelf environments (Matthews et al., 1997). During middle-Miocene time, local crustal contraction in the Nam Con Son Basin interrupted the extension and basin subsidence, creating several uplifted structures in the basin (Matthews et al., 1997; Olson, 2001). This mild crustal deformation was broadly synchronous with the regional inversion in the West Natuna basin (Matthews et al., 1997). From the Pliocene until the present thermal subsidence is interpreted to be the main control on basin development.

The geometry of the Nam Con Son Basin is approximately 350 km long, 200 km wide and as much as 13 km deep. The basin was deformed by a complex normal fault system with dominant trends to the N-S, E-W and NE-SW. In the western part of the basin, N-S faults are developed most strongly. The E-W trending system is observed mostly in the south east, while the NE-SW faults are dominant in the east (Matthews et al., 1997).
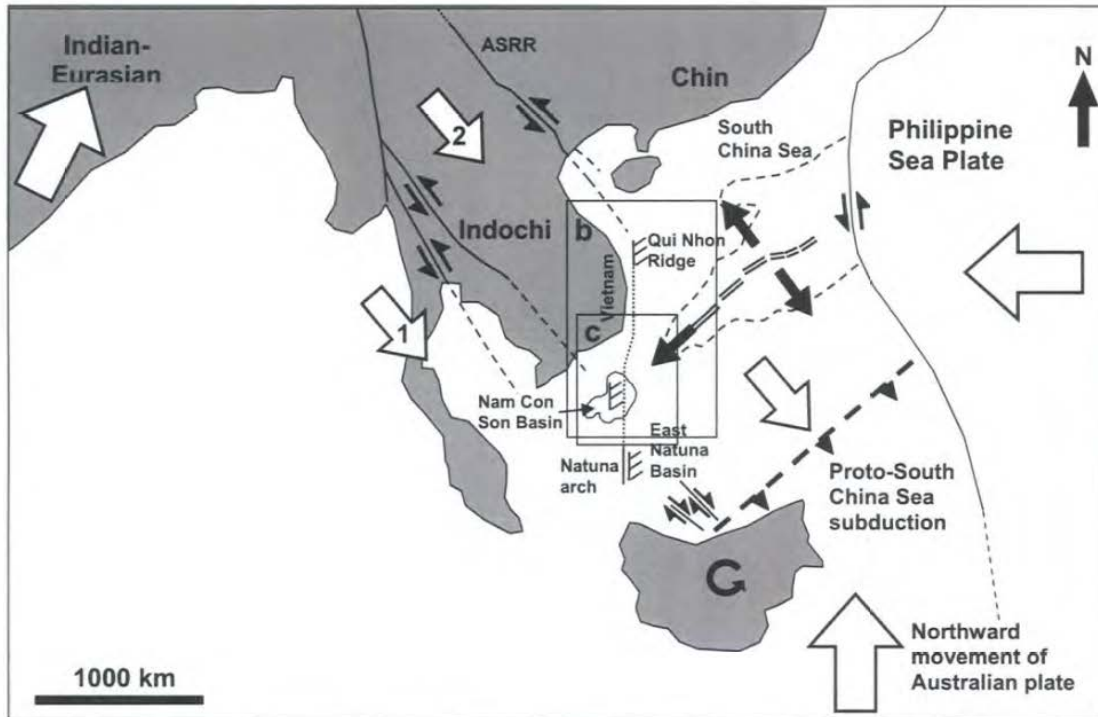
Figure 2.1: Location of the Nam Con Son basin and regional tectonic elements (Pugh, 2007). Tectonic displacements are represented by the large arrows.

2.2 General Stratigraphy of the Nam Con Son Basin

Previous studies and recent exploration show that the strata of the Nam Con Son basin comprises seven major lithostratigraphic units which are: 1) an unnamed Eocene unit, 2) the Oligocene Cau Formation, 3) the lower Miocene Dua Formation, 4) the middle Miocene Thong Formation, 5) the middle Miocene Mang Cau Formation, 6) the upper Miocene Nam Con Son Formation, and 7) the Pliocene to Recent Bien Dong Formation (Matthews et al., 1997). These seven units overlie the pre-Tertiary basement that has been penetrated by several wells on structural highs and described as an assemblage of volcanic, igneous and meta-sedimentary rocks.
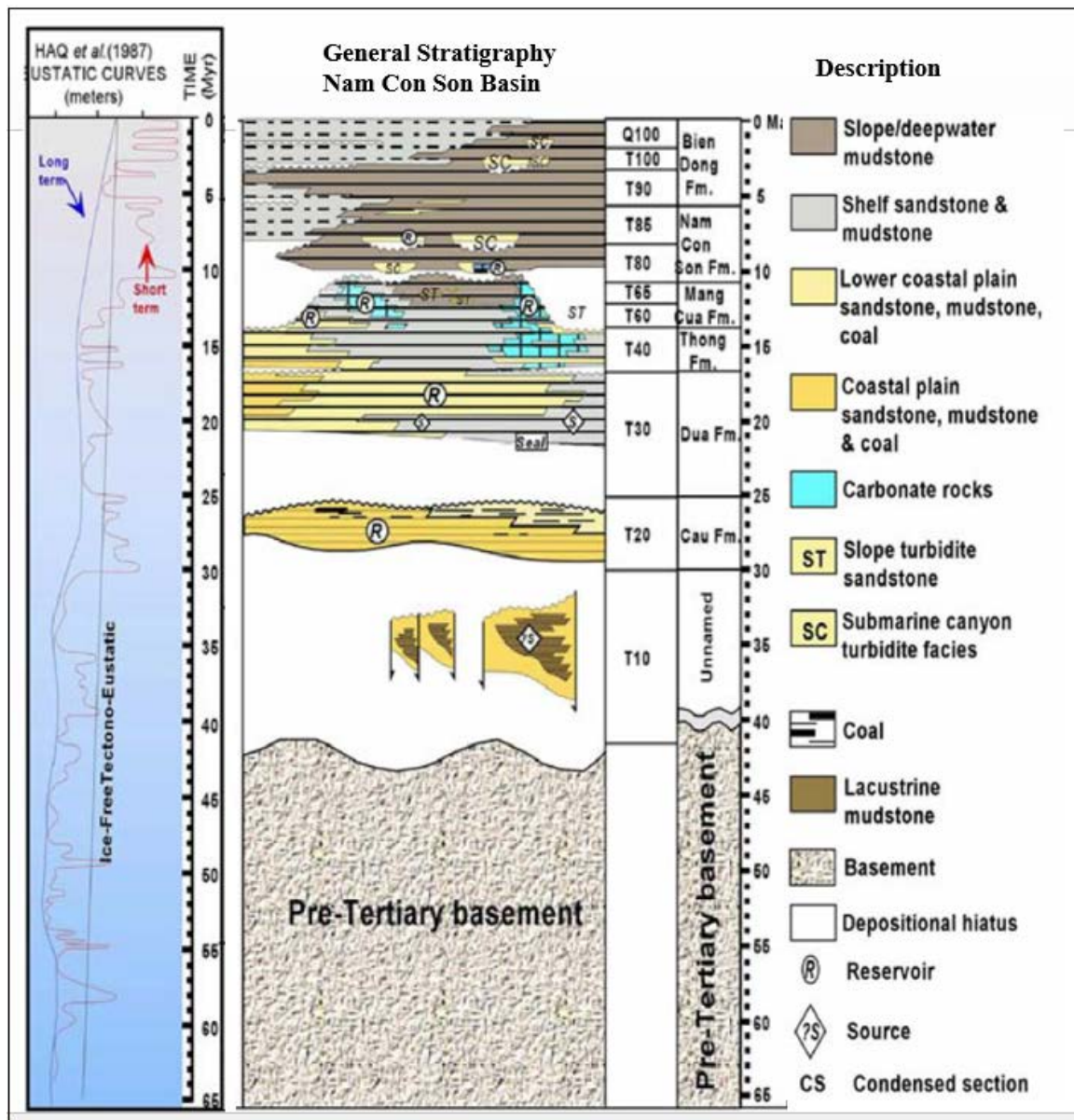
7

Figure 2.2: a) Chronostratigraphy of Nam Con Son Basin (Matthews et al., 1997 & Olson, 2001). Eustatic sea level curve from Haq et al., 1987.

The Eocene to lower-Oligocene sequences of the Nam Con Son basin are not formally named and are poorly understood. Based on analogues in the adjacent area (Sladen 1993), this sequence is composed of syn-rift conglomerate and coarse

8

grained-sandstone that were deposited in a fluvial-lacustrine environment (Matthews et al., 1997). The Oligocene Cau Formation is characterized by coarse-grained sandstone with thin layers of coal, claystone, and siltstone that were deposited in backstepping fluvial-deltaic facies with minimal tidal influence (Bat, 1993). During the deposition of this sequence, the basin underwent a thermal sag phase following the earlier rifting period. The study area is located in the vicinity of a structural high and does not contain the two formations mentioned above.

The Miocene sequences, which include the Dua, Thong and Mang Cau Formations, represent the deepest sedimentary sequences in the study area. These sequences were deposited in N-S and NE-SW-trending graben and represent the main syn-rift phase. The top of this syn-rift sequence is defined by a regional unconformity that has eroded the footwall and is associated with major channels and scours that locally truncate the Miocene rift faults (Matthews et al., 1997). This regional unconformity has age of upper- Middle Miocence and probably associated with a major eustatic sea-level fall at 10.5 Ma (Haq et al., 1987).

The lower-Miocene Dua Formation with stacked sandstone reservoirs is known as the main producing units in Nam Con Son basin. The lowermost sediments of Dua formation are defined as thin transgressive sandstone and marine claystone. Que (1993) documented that upper Dua Formation is composed mainly of claystone with sparse thin layers of sandstone and coal. The Dua Formation has total thickness ranging from 700 to 900 m. The lower unit was deposited in a fluvial-deltaic environment while the basin experienced a gradual transition to open marine shelf

environments for the upper Dua Formation (Que, 1993). The top of this sequence is marked by an onlap surface representing a shift from fluvio-deltaic facies below to shelfal marine clastics and carbonates above (Matthews et al., 1997).

The middle-Miocene Thong Formation consists of poorly sorted sandstone with thin layers of calcareous claystone (Bat et al., 1993). The depositional environment was controlled by the bathymetric variation in middle Miocene rifting phase. The eastern side of the Nam Con Son sub-basin subsided at a higher rate than its western side, which is apparent from the upper part of the Thong Formation. Carbonate shelfal sediments were deposited in marginal to non-marine environments in the west and they pass basinward into mudstones in deeper marine environments existed in some areas to the east of the basin (Matthews et al., 1997).

The middle-Miocene Mang Cau Formation can be separated into lower and upper units (Bat et al., 1993). The lower unit consists of sandstone and carbonate-rich claystone that were deposited in predominantly shelfal environment. The upper part of this sequence is characterized by deeper water clastic sediments such as sandstone, packstone and calcareous claystone (Bat, 1993). The top of the upper Mang Cau Formation is marked with the prominent middle Miocene unconformity (MMU) which was formed during a major eustatic lowstand (Haq et al., 1997). The MMU was enhanced by tectonic uplift and inversion across the southern and eastern parts of the Nam Con Son basin (Olson, 2001).

The lower part of Nam Con Son Formation was deposited in early Late Miocene and characterized by calcareous mudstone, claystone, and thin layers of sandstone (Bat et

al., 1993; Que, 1993). The top of the lower unit represent a basinward shift into deeper water settings (Matthews's el.al, 1997). The overlying upper part consists of shelf and slope clastics and some carbonate to the west. Deepwater mudstones that are preserved between carbonate build-ups occur mostly to the east. The Nam Con Son Formation represents the major phase of middle Miocene carbonate sedimentation in the basin and was terminated by the upper-Miocene unconformity (UMU) (Matthews et al., 1997).

The Bien Dong Formation which was deposited during Pliocene to recent time is the youngest sedimentary sequence in Nam Con Son basin. In general, the formation is characterized by shelf clastics in the west and slope deposits throughout the eastern parts (Matthews et al., 1997). Bat (1993) documented that the common sedimentary rocks are mudstone, siltstone and turbiditic sands. The paleo- Mekong River was interpreted as the main sedimentary sources for the Nam Con Son basin during Pliocene to Recent time (Murray and Dorobek, 2004). At this time the paleo-Mekong River delta quickly prograded across the Con Son High and the influx of terriginous clastic sediments terminated the carbonate sedimentation within the Nam Con Son basin (Matthews et al., 1997).

2.3 The Study area

The study area is located on the crest of a major northeast trending, tilted fault block in the Nam Con Son basin (Figures 2.3). It contains several stacked reservoir sequences with granitic basement at a depth of 2600 m in the shallowest part of the field. Overlying directly above the basement is the Early Miocene clastic sedimentary sequence with thickness of approximately 800 m.
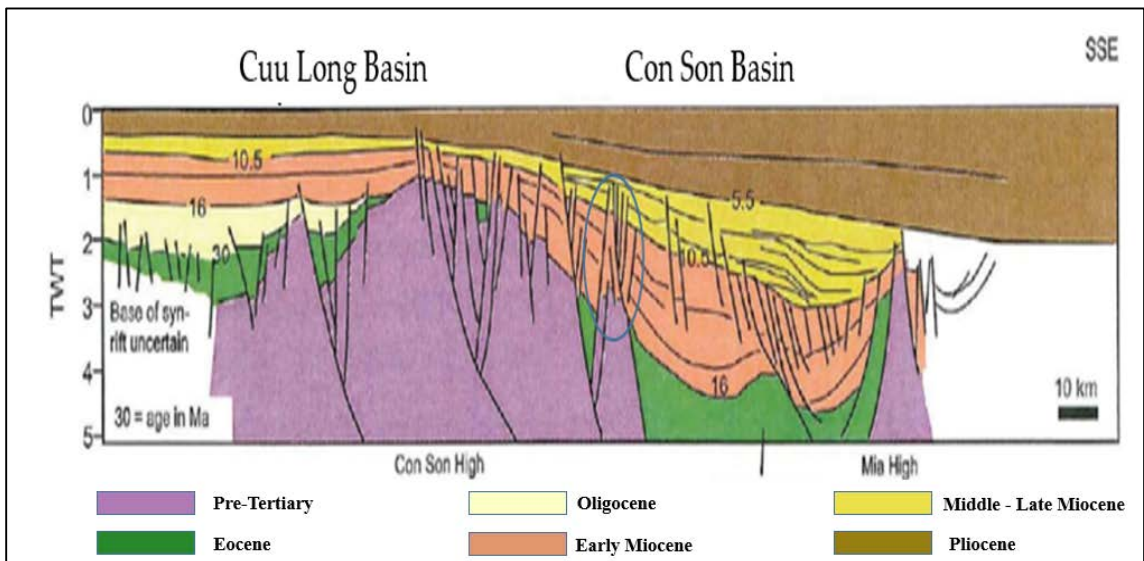

Figure 2.3: Geologic cross section in NNW-SSE direction showing approximate location of the study area in the Nam Con Son basin (Modified from DH report, PVEP, 2006)

The structure is bounded along its eastern side by a system of large-displacement normal faults that are down-thrown to the southeast. The field is bounded along its western flank by a number of normal faults that are down-thrown to the northwest. The overall shape of the field is similar to a narrow dome, stretching in a northeast-southwest direction and bounded by the faults described above.

The field is strongly compartmentalized internally, by normal faults that strike generally to the northwest and northeast. Northeast-trending normal faults, most of which

12

dip west, were active at two periods during the deposition of the clastic sediments. Both sets of northwest-striking faults were active synchronously during the second period of faulting. Following this, a region-wide erosional surface was developed across the top of the clastic sequence. The carbonate platform that was established above this unconformity was mildly influenced by drape over the underlying fault blocks and minor offsets on some of the faults.

A major period of faulting during the middle-Miocene resulted in the study area being tilted to the northwest and the carbonates being progressively on-lapped from the northwest by a younger sequence of mud-dominated clastic sediments. The main northeast-trending fault system that serves as the eastern boundary of the field was active at this time. Many of the northeast-trending faults were reactivated, and, in addition, a number of northwest-trending faults became active and separated the field into smaller blocks. Faulting gradually died out during the late Miocene and early Pliocene as the field was buried beneath clastic sediments that attain a thickness of at least 2000 m in response to a tectonic event that tilted the basin to the southeast.

The main targets of this study are the thin, hydrocarbon-bearing sandstones of the Miocene Dua Formation (Figure 4). These sandstones are interbedded with claystones and thin layer of coal, generating complex reflectivity patterns and causing interference effects such that they are almost impossible to be mapped on the original seismic data. Previous studies have shown that the main faults separating the blocks are sealing faults. This sealing ability is largely attributed to the large proportion of mudstone in the reservoir sequence and the occurrence of numerous, relatively thin, sandstone units

(Matthews et al., 1997). Thus there is abundant material available to provide effective clay smearing on fault surfaces.

It must be recognized that in this area there are a considerable amount of small-throw faults with displacements close to and below the seismic resolution of the conventional seismic data. Examination of the 3D seismic data shows that there are numerous small flexures in some reflections. It is highly probable that some of these are small faults with displacement of 20 m or less, and thus below the resolution of the conventional seismic data, that could influence sand-on-sand contacts and hence have an impact on production efficiency. Therefore there is an important need for improving the seismic resolution to better image the thin sands and small-throw faults in this area.
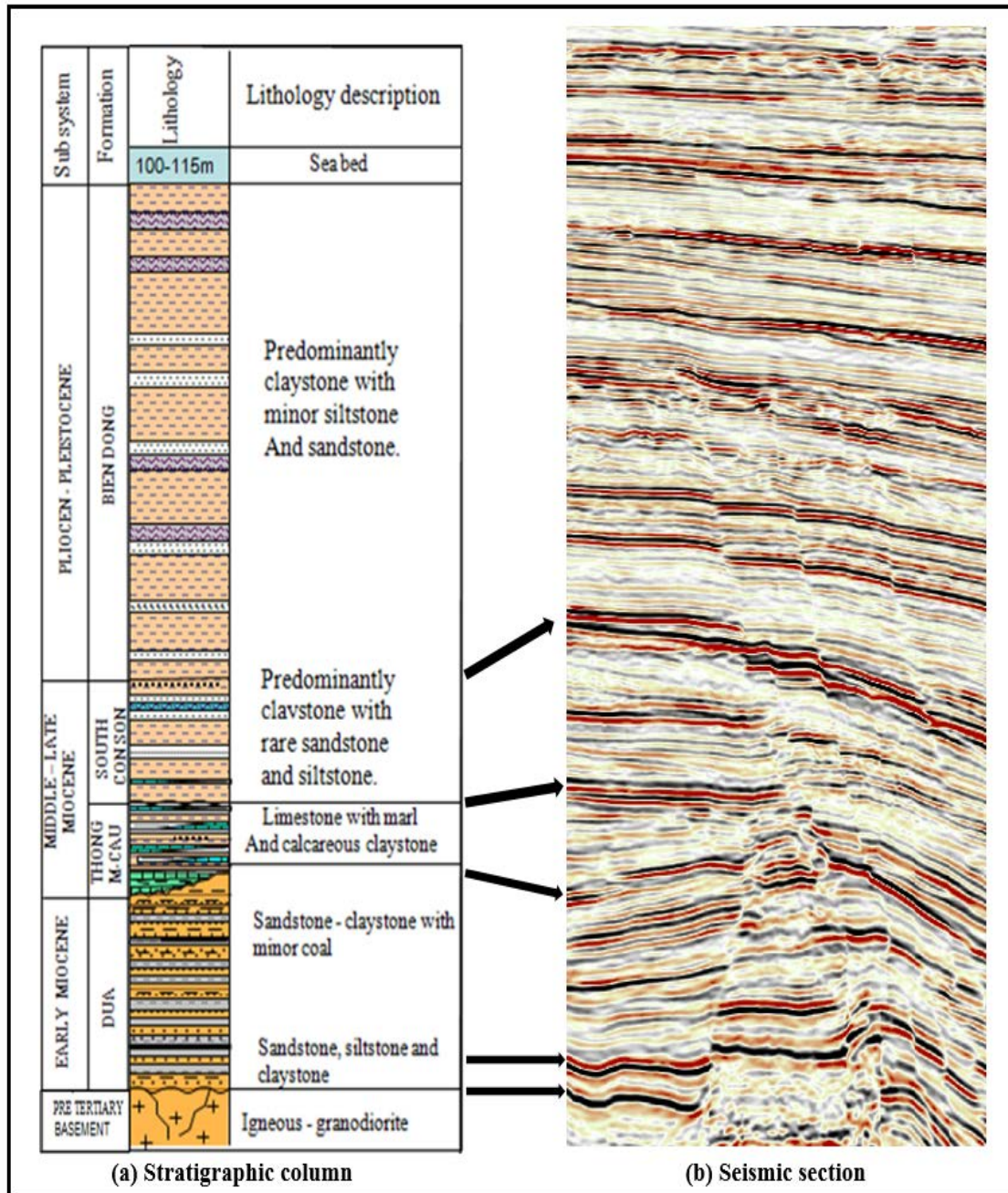
Figure 2.4: Seismic stratigraphy on a section through well C. (a) Stratigraphic chart was modified from DH report, PVEP (2006). (b) A vertical section with approximate location of the geological boundaries.

15

3. THEORY

This section reviews the basic knowledge of spectral decomposition, spectral inversion and wavelet deconvolution to better understand how this method improves the resolution of seismic data.

3.1 Spectral Decomposition

Spectral decomposition transforms the reflection seismogram into a time-frequency space that represents localized frequency content occurring as a function of record time (Castagna, et al., 2003).

The concept of spectral decomposition is the foundation for thin-bed thickness estimation and spectral reflectivity inversion. Partyka et al. (1999) showed that the expression of a thin-bed seismic reflection in the frequency domain is indicative of its temporal thickness (Figure 3.1). The thin-bed frequency spectrum is similar to the source wavelet, except that it shows notches that are corresponding to local geological variability. The inverse relationship between the periodicity of the notches and the temporal thickness of thin layer (Gridley and Partyka, 1997) facilitates the ability for thickness to be estimated from spectral analysis of seismic response.
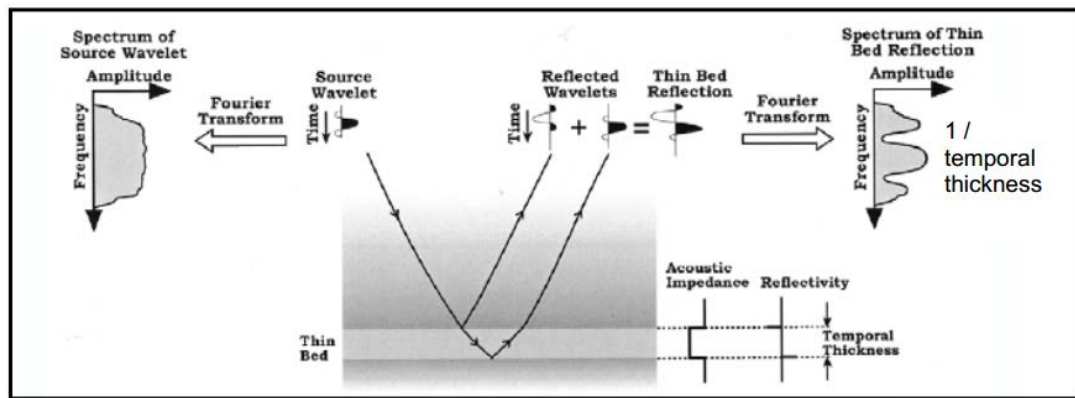
Figure 3.1: Thin-bed model and spectral imaging (from Partyka et al., 1999)

An important factor in the results of the transform is the size of the window. A long window samples many layers, which tends to approximate the spectrum of the source wavelet and suppress the desired geologic information (Figure 3.2). A short window samples fewer layers and provides better geological details (Figure 3.3). The resulting spectrum shows the general overprint of the source wavelet with notching pattern representing rock layering within the window (Partyka, 1999).

Windowing the seismic trace for spectral decomposition requires proper understanding of its effects. When the window is long enough to allow interference between composite wavelets within the window, the time resolution will be reduced because of averaging effect. The opposite problem arises when too short a window is used to isolate a reflection in time. A short window results in better resolution and allows capturing of local geological information; however the frequency resolution is compromised due to spectral smearing.
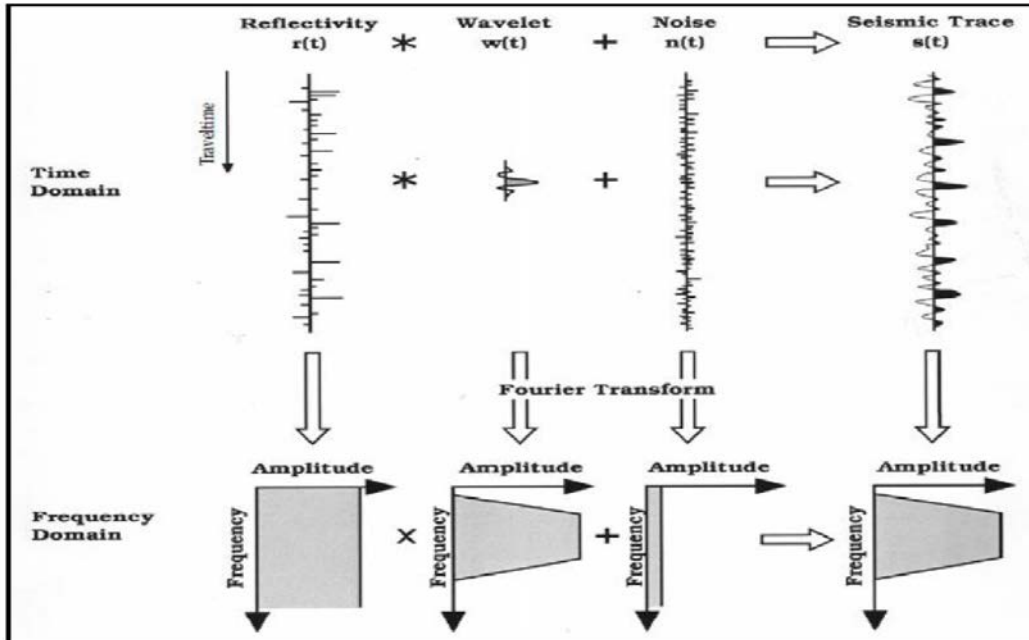
Figure 3.2: Long time window spectral decomposition showing a flat (white) amplitude spectrum. The layering of the geology is considered random and the spectrum of the trace is overprinted by the wavelet spectrum (Partyka et al., 1999).
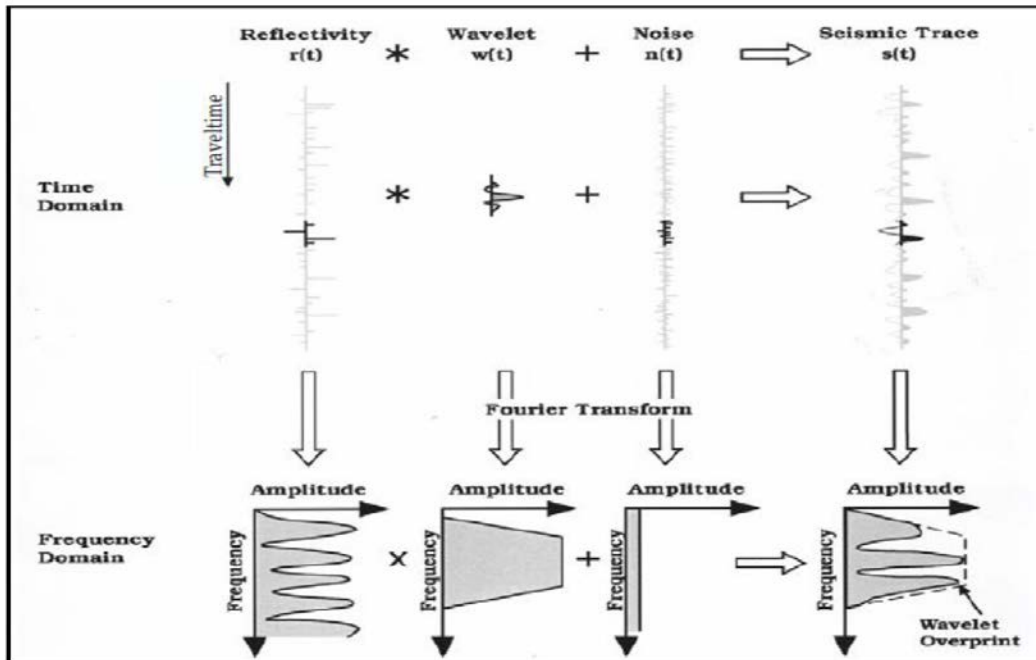

Figure 3.3: Short time window spectral decomposition showing a notched amplitude spectrum. The amplitude spectrum of the seismic trace will preserve the local layering properties within the window (Partyka et al., 1999).

Many methods for spectral decomposition have been previously described and analyzed by Chakraborty and Okaya (1995), Castagna et al. (2003), Castagna and Sun (2006) and Puryear (2012). Spectral decomposition is non-unique and each method has advantages and disadvantages. In order to use the spectral analysis for layer thickness estimation, precision is needed in both the frequency domain (in order to resolve the thickness) and in the time domain (in order to predict its location in time). Using a short time Fourier Transform (STFT) gives better time resolution but the spectral resolution is smeared as a result of poor frequency resolution. An alternative approach is the continuous wavelet transform (CWT), which is equivalent to temporal narrow-band filtering of the seismic trace using stretched version of a mother wavelet. The semi-orthogonal Morlet wavelet is commonly used for seismic application (Castagna and Sun, 2006). Both of these methods require that for higher frequency resolution, temporal resolution is sacrificed and vice versa. This time-frequency resolution tradeoff, known as Heisenberg uncertainty principle, causes spectral smearing and creates difficulties for the detection of thin-beds.

An inversion-based spectral decomposition method was introduced by Puryear (2012), called constrained least-squares spectral analysis (CLSSA). This method uses "prior" geologic information instead of mathematical assumptions, as constraints to achieve a unique solution. It computes the spectrum of a windowed portion of a seismic signal by finding a sparse weighted summation of truncated sinusoids that reconstruct the signal. Fourier series coefficients were then determined based on the weights of the sinusoids. Puryear (2012) show that CLSSA has significantly improved the time-frequency

19

resolution tradeoff, and reduces spectral smearing compared to conventional methods (Figure 3.4). Thus it enables better determination of the spectral characteristics of interfering reflections within a short time window.
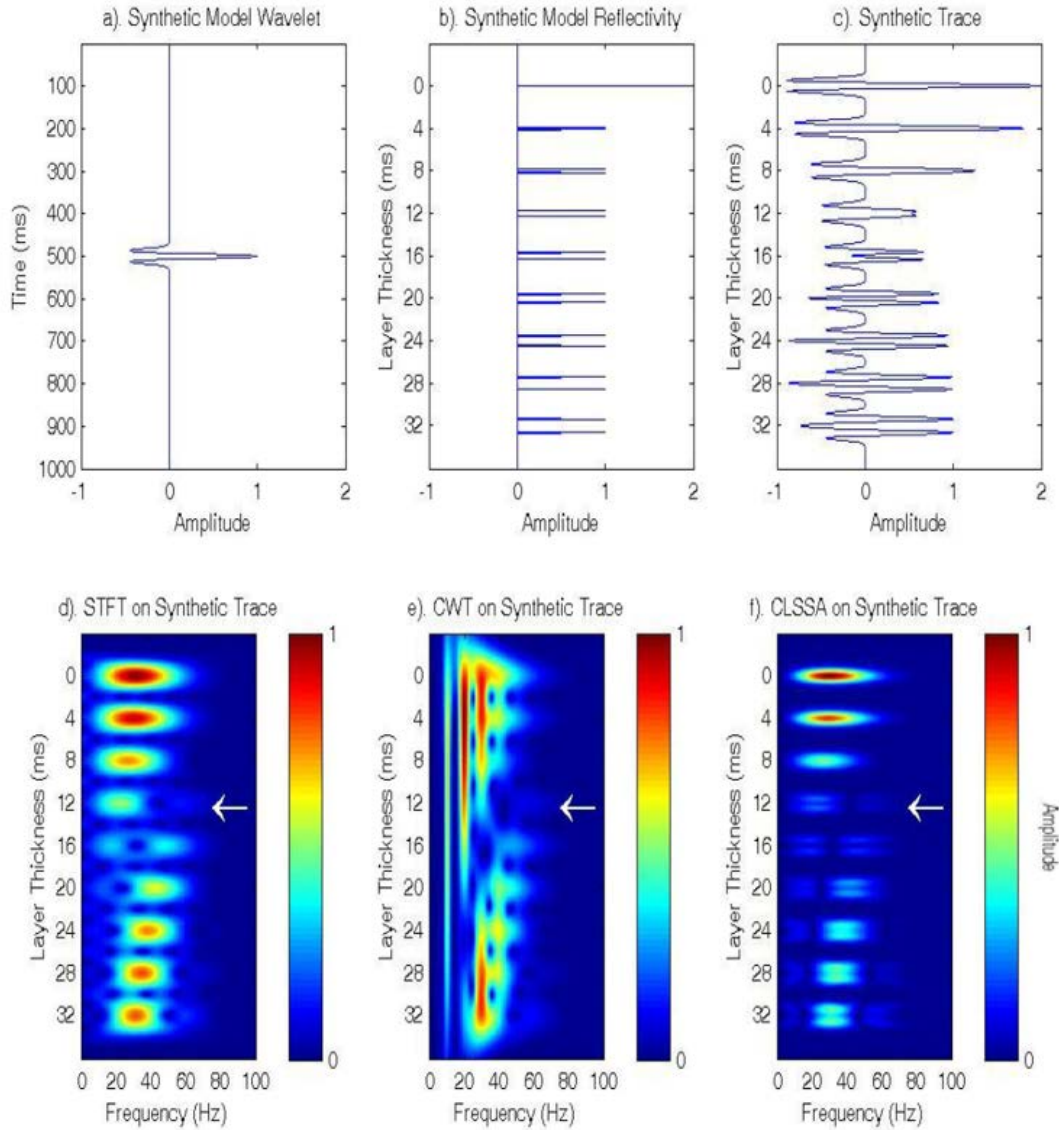

Figure 3.4: Comparison of spectral decomposition methods using synthetic model of even reflectivity pairs a) STFT with 40 ms window, b) CWT using Morlet wavelet dictionary, c) CLSSA using 40 ms window. CLSSA shows much sharper spectral notches defining thin-bed dipoles in the time domain. Layers with temporal thickness of approximately 12 ms can be separated at high frequencies (arrow). Illustrations after Puryear (2012).

3.2 Spectral Inversion Theory

Partyka first used the term "spectral inversion" in 2005 for the procedure of thin-bed inversion in the frequency domain. The inversion for layer thickness utilizes the inverse relationship between thickness and constant periodicity of spectral interference patterns to delineate accurate thickness estimation below tuning.

Spectral inversion uses the general reflectivity model that is different from conventional Widess model. The Widess model (1973) assumes a perfectly odd pair of reflection coefficients with an equal magnitude and opposite sign, resulting in maximum destructive interference of reflections of beds with thickness less than $\lambda/8$, where λ is defined as the dominant wavelength (Figure 3.5). The theoretical limit for seismic vertical resolution is determined as $\lambda/8$ and in the presence of noise, the practical resolution reduces to $\lambda/4$. Because of the destructive interference of the waveforms at the top and bottom of a thin layer, amplitude of the reflections reached its maximum as the bed thickness approaches the tuning thickness ($\lambda/4$), and then diminishes towards zero thickness (Figure 3.6).
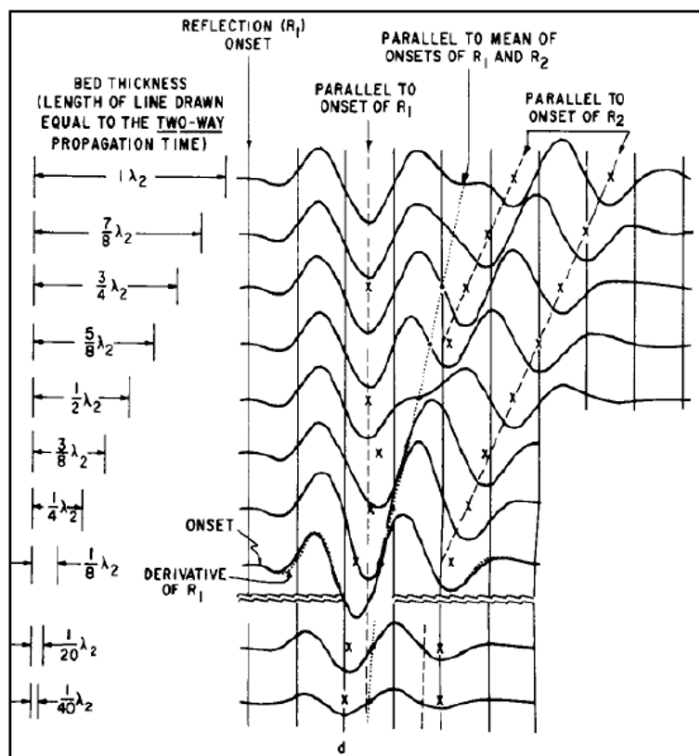
Figure 3.5: Wedge model showing the resulting seismic reflection as changing layer thickness. Below λ/8, the waveform shape does not change significantly but amplitude steadily diminishes (Widess, 1973).
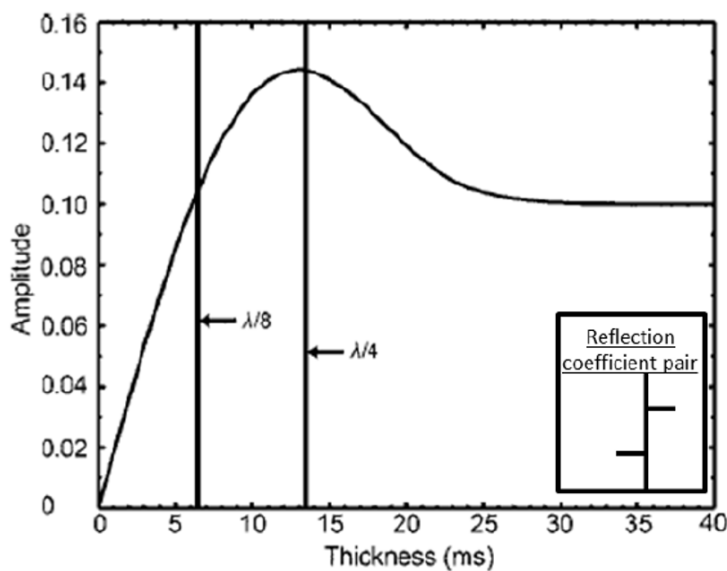

Figure 3.6: Amplitude versus thickness. Amplitude increases as thickness approaches λ/4. Below this tuning thickness, amplitude decreases nearly linearly toward zero thickness (from Puryear and Castagna, 2008)

Recent studies (Tirado, 2004; Portniaguine and Castagna, 2005; Castagna, 2005; Chopra, et al., 2006; Puryear and Castagna, 2008) explain how the theoretical resolution limit extends further than $\lambda/8$, where the seismic amplitude and frequency response is more sensitive for beds of sub-tuning thickness. Another view of the reflection pairs was proposed by Tirado (2004), which potentially improves thickness estimations. Any pair of reflection coefficients, representing the top and bottom of a thin-bed, can be decomposed into a pair of even components and a pair of odd components. The even reflection coefficient pair has the same polarity and magnitudes, whereas the odd pair has the same magnitude but opposite polarity.
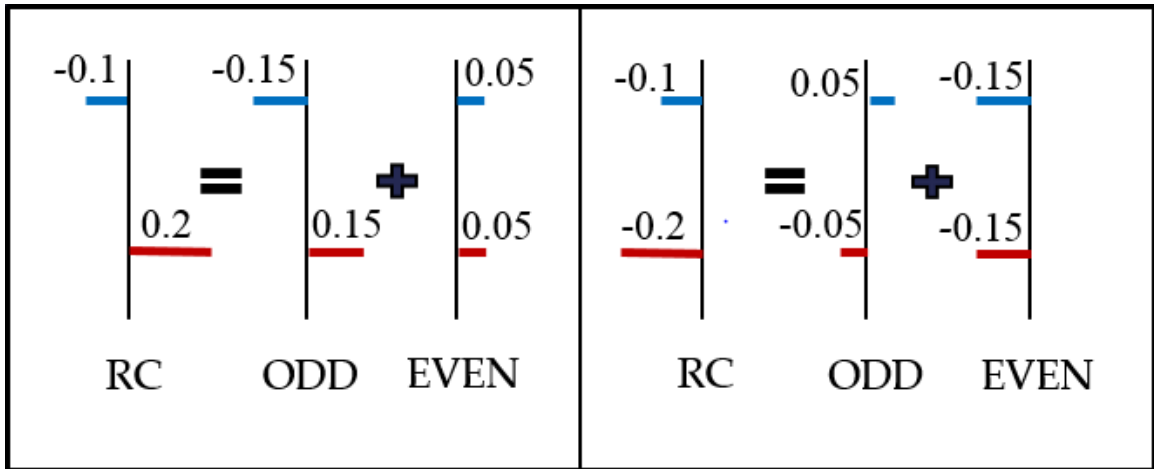

Figure 3.7: Two examples of a pair of arbitrary reflection coefficients representing thin-beds. Any reflection coefficients pair can be decomposed into odd and even components. The odd component has opposite polarity and the same magnitude, while the even component has the same polarity and magnitude (Modified from Rodriguez, 2009).

The analysis of peak amplitudes vs thickness for each of these components (odd and even) shows that the odd component behaves similarly to the Widess model (Figure 3.8, right panel). The maximum amplitude is reached at tuning thickness ($\lambda/4$) and then interferes destructively and cancels itself as thickness decrease to zero. In contrast, the

23

even component becomes more important below $\lambda/8$ and behaves just the opposite way. Due to constructive interference, the even component of successive reflector adds more signal on down to zero thickness. The total amplitude of the reflection is closer to the even component and does not diminishes to zero as suggested by Widess model. Therefore it significantly contributes to the thickness estimation of thin-beds below tuning thickness.

The peak-frequency analysis vs. thickness (Figure 3.8, left panel) shows that the odd and even components behave differently with layer thickness ranging from zero to $\lambda/8$. The peak frequency of odd component, similar to the Widess model, remains almost constant when thickness reduces from $\lambda/8$ to zero. In contrast the even component reaches it maximum at $\lambda/8$ and decreases as thickness is reduced to zero. The total peak frequency gradually increases, as thickness decreases, but below a certain thickness (close to $\lambda/8$), the peak frequency changes and approaches the same peak frequency of the event component. This frequency is equivalent to the frequency of the wavelet instead of its derivative (Chopra et al., 2006, Puryear and Castagna, 2008). According to the above analysis we infer that the seismic data response is more sensitive to thin-beds than previously thought (Chopra et al., 2006). The amplitude and frequency components vary beyond the theoretical limit of seismic resolution ($\lambda/8$). The approach based on the general reflectivity model and spectral decomposition potentially allows thicknesses below the resolution limit of the bandwidth to be recovered.
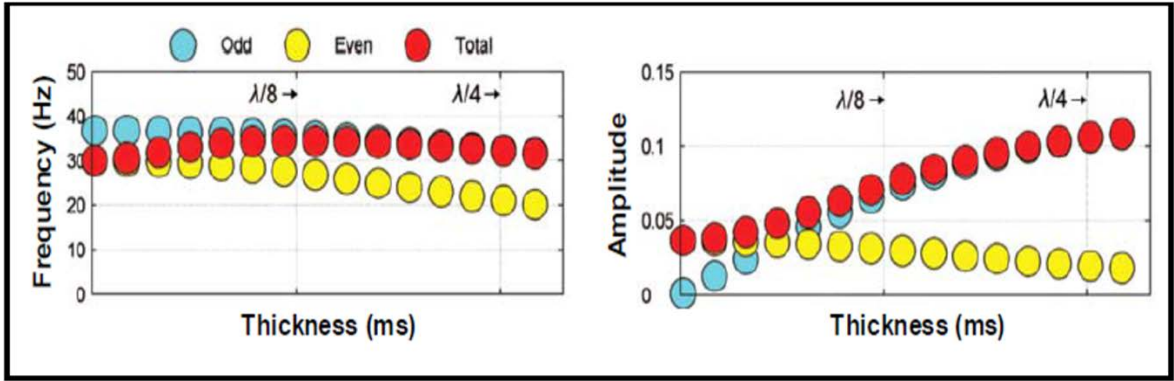
Figure 3.8: Peak frequency (left) and peak amplitude (right) as a function of temporal thickness for the even and odd components, as well as the total. There is peak amplitude and frequency information below the tuning thickness. The total peak amplitude comes close to the even component amplitude (from Puryear and Castagna, 2008).

Portniaguine and Castagna (2005) discussed a post-stack inversion method to resolve thin layers. First the well control is used to estimate the time and spatially- varying wavelets from the data. If no well control is available, a statistical wavelet extraction method needs to be used (Chopra et al., 2006). Secondly, the wavelets are removed from the data with a seismic inversion process which utilizes the concept of spectral decomposition. This inversion method was performed trace by trace, hence it is unbiased by lateral continuity constraints from an initial model based on well logs and horizons. However, available well data may provide useful control points to verify the quality of the results (Chopra et al., 2006).

Puryear and Castagna (2008) discussed the theory of spectral inversion and developed an algorithm to invert reflectivity. The algorithm was developed by applying Fourier transforms in time windows to various reflectivity models and analyzing the amplitude spectrum for a layer of a given thickness. The notch period (in Hz) in the spectrum is inversely related to the layer temporal thickness (Partyka et al., 1999; Marfurt and Kirlin, 2001). The layer thickness can be predicted, given that the frequency band is broad

25

enough to resolve the periodicity and the data have high signal to noise ratio (Puryear and

Castagna, 2008).

A newly developed spectral inversion method also decomposes reflectivity into even

and odd components, and then it further extends them into even and odd wedge

dictionaries. The basis of this method, called sparse layer inversion was proposed by

Zhang and Castagna (2011). In general, it is a time-domain inversion using a basis pursuit

of a dictionary of functions representing thin-bed reflectivity patterns that sum together to
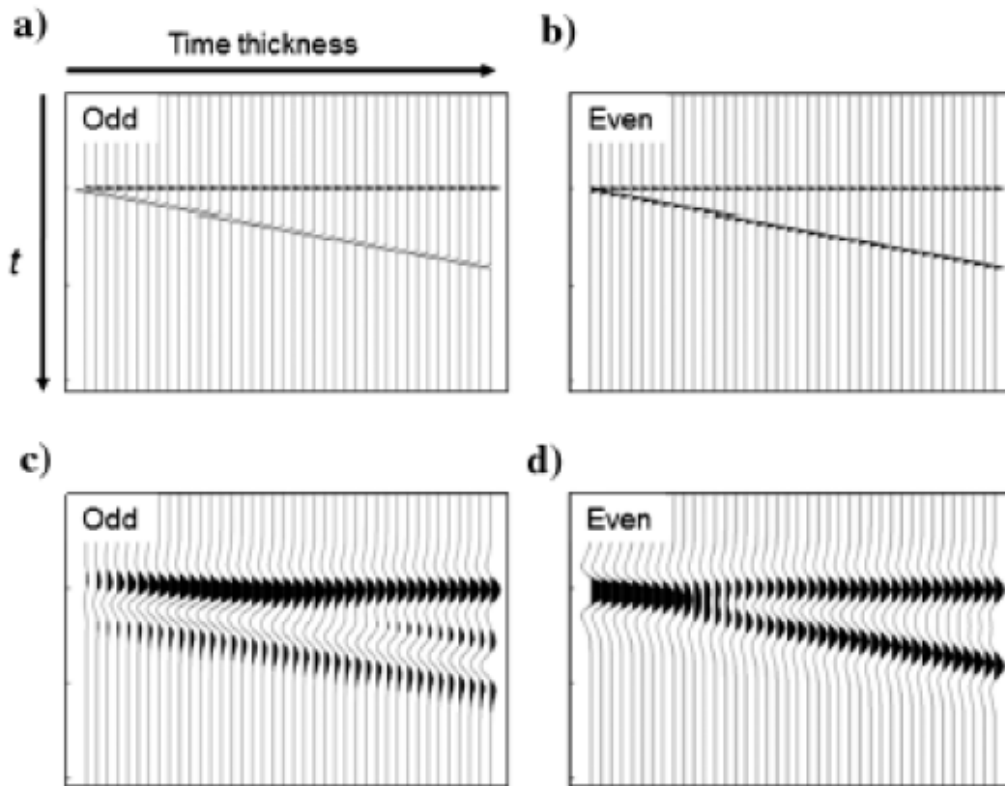
form the seismic trace (Zhang, 2011).

Figure 3.9: Wedge dictionaries are shown for the (a) odd and (b) even components of reflectivity. Their synthetic traces generated using a 30Hz Ricker wavelets are shown in (c) and (d) (From Zhang and Castagna, 2011).

To better understand the concept of sparse layer inversion, we start with the well-known convolution model, stating that a post-processing seismogram could be thought of as convolution of a reflectivity sequence representing sparse structured subsurface layers with embedded wavelets:

$$s(t) = w(t)* r(t) + n(t) \ (1)$$

where $s(t)$ is the seismic trace, $w(t)$ is the seismic wavelet, $r(t)$ is the reflectivity series, and $n(t)$ is the noise. This model assumes a layer-cake earth model represented adequately by a series of planar horizontal layers of constant impedance with reflections generated at the boundaries between adjacent layers. The seismic trace is the convolution of the reflectivity series with the seismic wavelet. Because seismic wavelets are band limited, the seismic trace always bear the source signature wavelet, which smears adjacent events and reduces the resolution of the image. Inversion of a seismic trace for reflectivity is understood in general to have the effect of increasing resolution or enhancing the frequency content.

The inversion of $s(t)$ for $r(t)$ with a known wavelet is non-unique. There are infinite numbers of reflectivity series that give the same seismic response. To find the "best" solution among all possibilities, additional information or constraints are required. Such constraints usually assume some prior information about the type of solution one desires. Different inversion methods will have different ways to incorporating the prior information into the inversion process, thus yielding different results.

When inverting the seismic convolution model to estimate broadband reflectivity, a sparse representation of the number of interfaces is a common choice because sparseness

27

leads to increased temporal detail and sharp interface definition. The commonly used sparse spike inversion (SSI) can produce sparse reflectivity series without the need for a starting model. This method limits the spacing between reflection coefficients to find a solution with a small numbers of layers. The sparse spike criterion gives a robust solution when the true geology contains only thick and blocky layers, however is potentially limited in its ability to resolve thin layers.

In comparison to sparse spike inversion, sparse layer inversion determines a sparse number of layer responses that can be summed together to form the seismic trace. Applying the sparseness criterion to layer responses rather than to individual interface responses produces a sparse reflectivity inversion that does not discriminate against thin layers (Mann, 2014). In addition, thickness information of sub-tuning beds that are obtained from spectral decomposition can be incorporated into the inversion. While how the spectral decomposition is employed into the inversion are proprietary, the constrained least-squares spectral analysis (CLSSA) can be used to spectrally decompose the seismic data which can then be applied as a constraint to sparse layer inversion.

3.3 Wavelet Deconvolution

Again we consider the convolutional model, where the seismic trace is the convolution of the wavelet w(t) and the reflectivity series r(t):

$$s(t) = w(t)* r(t) + n(t) \ (1)$$

Deconvolution is the process aiming to remove the effects of the seismic wavelet from the input seismic trace to yield the seismic reflectivity. In practice commonly only the seismic traces are available and we need to find both the wavelet and the reflectivity (Zhou, 2014). Statistical deconvolution, or predictive deconvolution, uses the autocorrelation of the trace to derive the deconvolution operator using the seismic data alone. This method cannot determine the correct phase independently so the phase of the deconvolution operator is assumed to be either zero-phase or minimum-phase. It also assumes that the reflection coefficients change randomly and the spectrum of the reflectivity series is white, which may not be the case of true geology.

When two of the three factors are known, the deconvolution becomes a deterministic process. Hampson-Russell software calls this approach wavelet deconvolution, which allows the design of an inverse operator from an extracted wavelet and applies that operator to the seismic data. The process aims to transform an input wavelet into a desired output shape. In theory the desired output is close to a single spike, however it is not achievable in reality. The wavelet deconvolution, however, should improve resolution of the data and the resulting seismic traces should be closer to the original reflection coefficients (Figure 3.10)

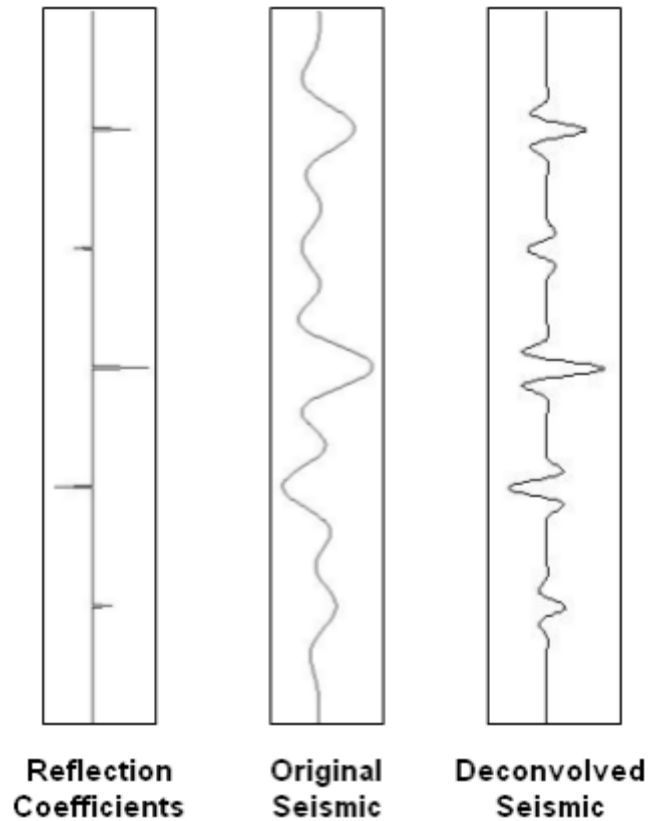Reflection Original Deconvolved
Coefficients Seismic Seismic

Figure 3.10: Result of deconvolution process. The wavelet effects are reduced and main reflections are sharper with smaller side lobes (Strata Theory, 2007).

In this study, wavelet deconvolution was applied using Hampson Russell software as an optional step to slightly improve the spectral inversion results before interpretation. Several tests were performed with various wavelet combination and parameters to yield the best solution. As the spectral inversion results were already high-frequency, a mild deconvolution effect was preferred.

4. RESULTS

All inversion methods for sparse-reflectivity contain frequency components outside the band of the original seismic data (Castagna, 2012). There are several other methods and algorithms to broaden the frequency range. However this bandwidth extension idea to recover the high frequencies using post-stack seismic data alone is controversial. Therefore this section will focus on validating the increased frequency content that may result from spectral inversion. Following that we will investigate how much the vertical resolution was improved, then attempt to assess and quantify the benefits of the high-resolution data on seismic interpretation. It must be recognized that the effectiveness of spectral inversion, or any other inversion methods, is dependent on many factors such as the original bandwidth of the data, the signal to noise ratio, estimation of the seismic wavelet, and also the complexity of the local geology.

4.1 Spectral Inversion Results

A comparison between the average frequency spectrum between the original seismic data and the spectral inversion result shows that the frequency bandwidth has been extended. A noticeable increase in amplitude for frequency range below 20 Hz and above 70 Hz was seen in the spectral inversion results, suggesting that the inversion process has recovered frequencies outside the range of the original seismic data.

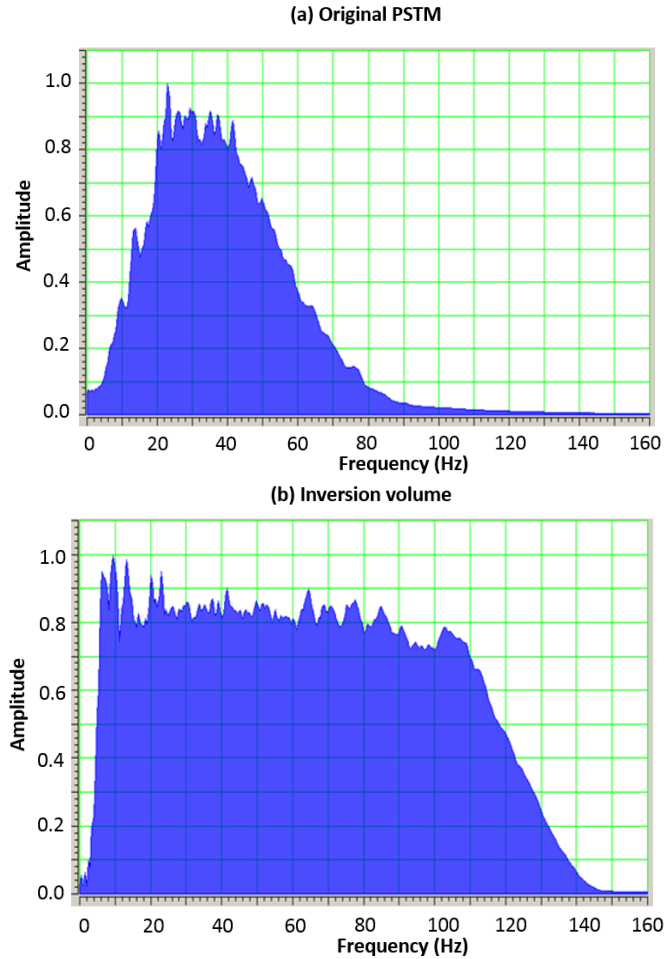**(a) Original PSTM**

(b) Inversion volume

Figure 4.1: Average amplitude spectrum of a) original PSTM data and b) spectral inversion data. The frequency bandwidth is broadened below 20 Hz and above 70 Hz

It is important to have a validation process of the inversion results as the frequency bandwidth of the seismic data is significantly expanded. The first step is to apply a common band-pass filter to both the PSTM data and the spectral inverted data. The band-pass filter needs to be designed so as to have similar frequency content to the original seismic data. In this case, a band-pass filter with a frequency range of 5-20-40-80 Hz, was applied to both seismic volumes. Both seismic sections seem to be very similar

(Figure 4.2). We may deduce from this comparison that the spectral inversion process does not appear to be have added any noise or artifacts to the original frequency range.
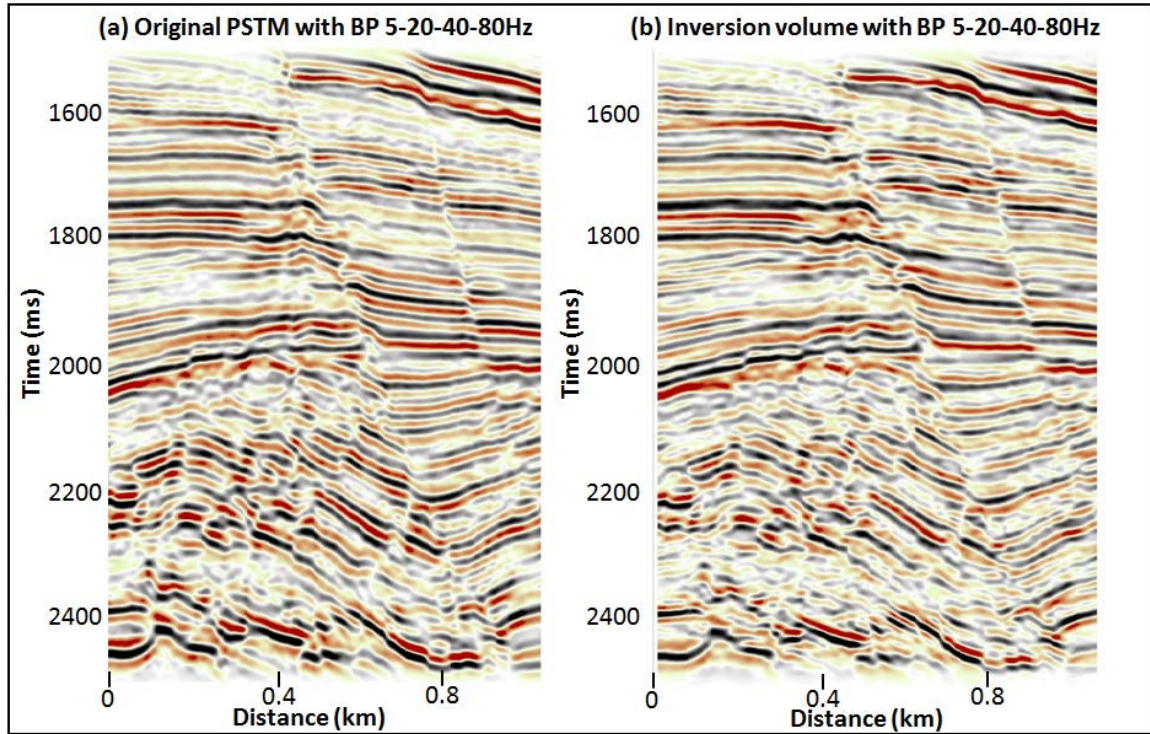

Figure 4.2: Comparison of the original PSTM and inversion volume with a bandpass filter of 5-20-40-80 Hz. The seismic sections are very similar. Peaks (positive amplitude) are black; troughs (negative amplitude) are red.

The next step involves establishing a desired bandwidth for the inversion data. As the signal to noise ratio is unknown, numerous bandpass filters were applied to the inversion data to determine within which frequency range the signal is usable. The data were scanned for different frequency ranges (10 Hz frequency increment) for the extra frequency content not available in the orginal data. Each frequency range was displayed and compared until we found the limit at which lateral coherence is no longer observed. Figure 4.3 shows the original data and the inversion data within two different frequency ranges of 90-100 Hz and 100-110 Hz, respectively. It appears that the lateral coherence is

33

preserved at the reservoir level for the data within the 90-100 Hz range, while it appears

to be greatly diminished in the 100-110 Hz range. We infer that this lack of lateral

coherence is related to the phase dirtortion of high-frequency content. The data of this

frequency range (100-110 Hz) and above are not consistent in terms of phase with the

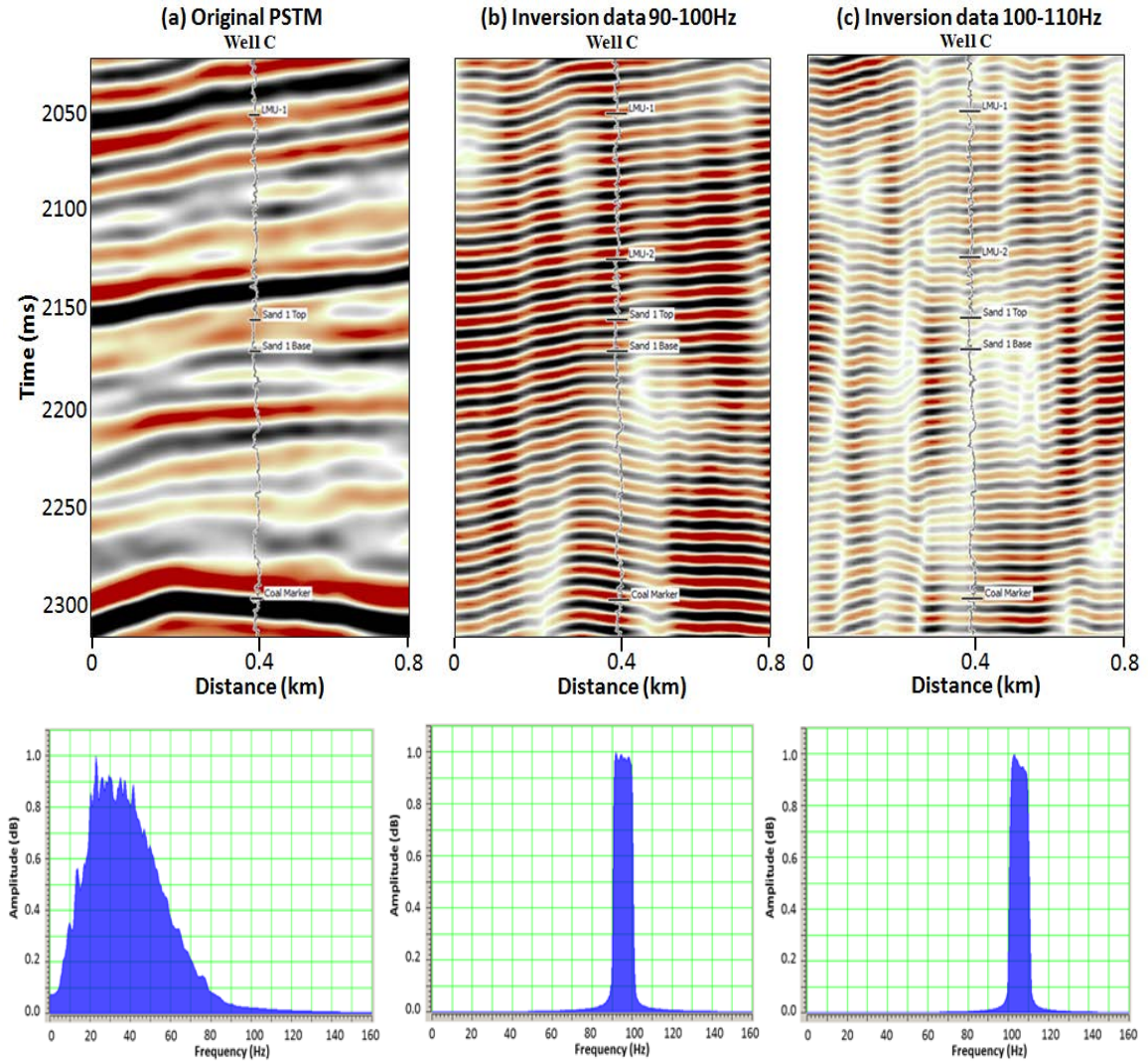low frequency content, and thus need to be removed.

Figure 4.3: Seismic sections and amplitude spectra of a) Original PSTM data
b) Spectral inversion data with frequency content of 90-100 Hz c) Spectral inversion data
with frequency content of 100-110 Hz. Peaks (positive amplitude) are black; troughs
(negative amplitude) are red.

34

It is more difficult to establish the limit on the low end of the frequency spectrum. As can be seen in Figure 4.4, the frequency content from 5-10 Hz show inconsistency with the geology observed in original PSTM data (arrow) and should not be included in the data.
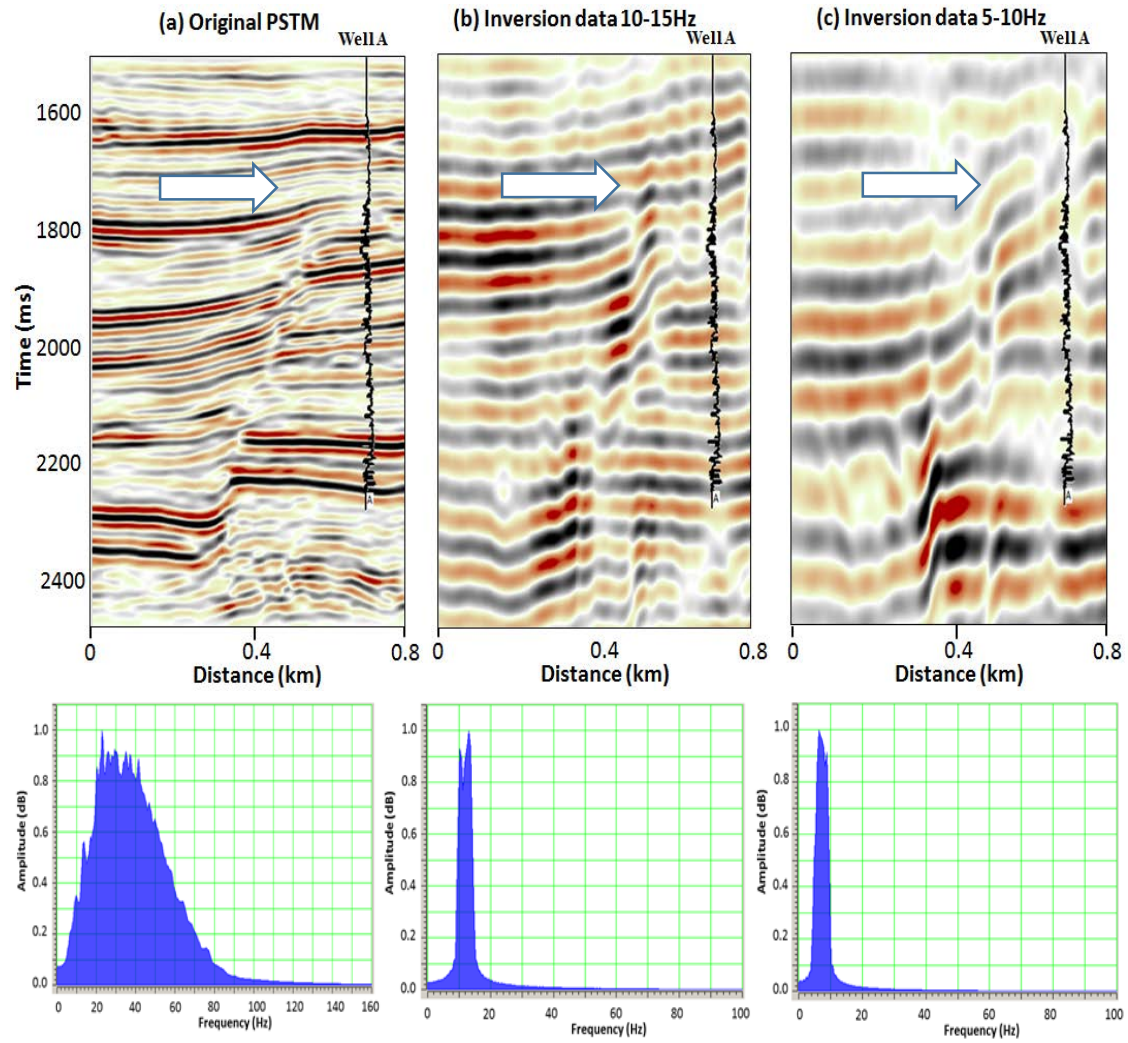

Figure 4.4: Seismic sections and amplitude spectra of a) Original PSTM data b) Spectral inversion data with frequency content of 10-15 Hz c) Spectral inversion data with frequency content of 5-10 Hz. Peaks (positive amplitude) are black; troughs (negative amplitude) are red.

The bandpass filtering analysis for each frequency range above suggests that the useful bandwidth with good signal to noise ratio and stable seismic phase is from 10 to 100 Hz. A final bandpass filter with low pass of 10 Hz and high pass of 100 Hz was applied to obtain the desired bandwidth. It can be seen that the filtered version (10-100 Hz) of spectral inversion data provides more continous events than the unfiltered version while still shows superior resolution compared to the original data (Figure 4.5).
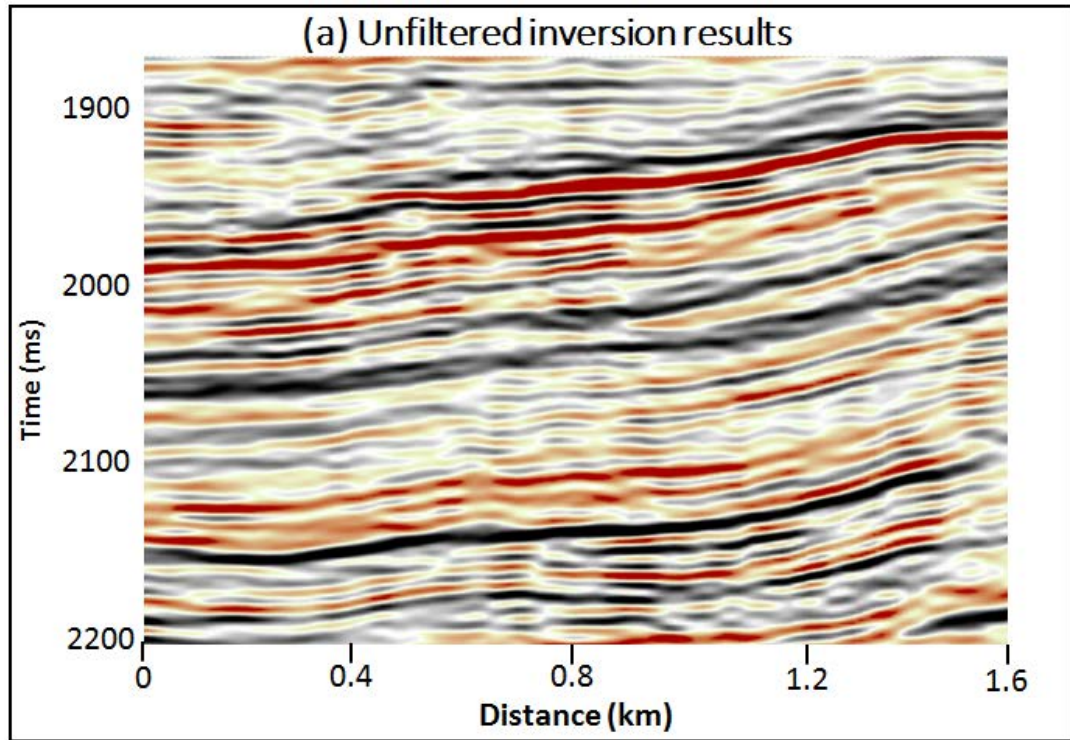
Figure 4.5: Seismic sections of (a) unfiltered spectral inversion results. Peaks (positive amplitude) are black; troughs (negative amplitude) are red.
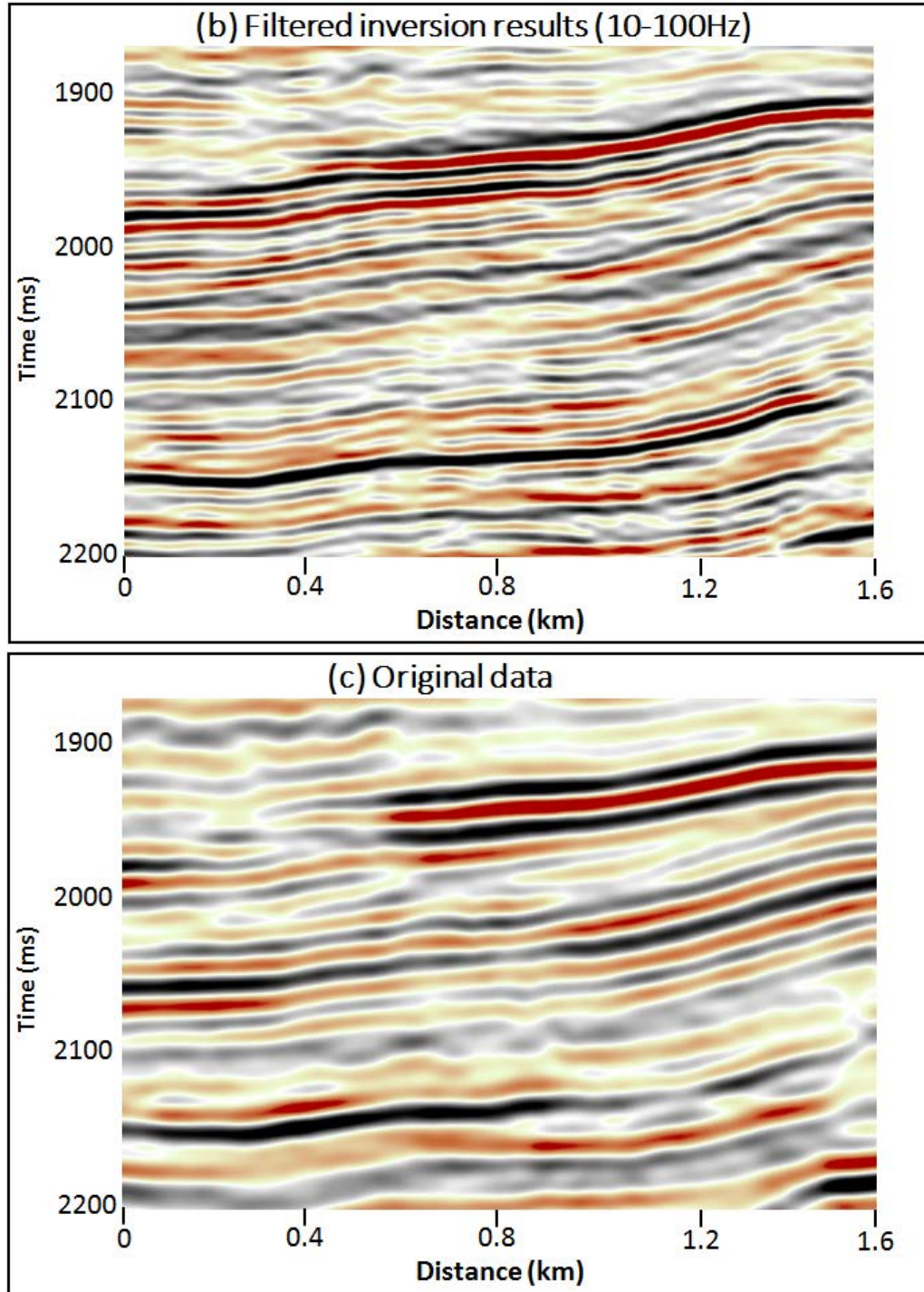
Figure 4.5 (cont): Seismic sections of (b) filtered inversion data (10-100 Hz) and (c) original PSTM data. The filtered version provides clean image with continuous events while still shows great improvement in vertical resolution compared to original data.

The second validation step was performed by doing well correlations with the high-resolution data. Figures 4.6, 4.7 and 4.8 illustrate side-by-side comparisons of two seismic volumes against synthetic seismograms derived from three wells. This is another way to visualize the improvements in the vertical resolution and consistency of the inversion process. A set of well logs (Gamma Ray, Density, P-wave velocity) and two seismic sections with their respective synthetic seismograms for different frequency ranges are displayed.

Because the frequency content of the inversion results are beyond the original data bandwidth, the spectral inversion process has recovered information that was not available in the original data, thus extra reflections appear in the high-resolution data. The extra events from the increased frequency content were verified by comparison to the well logs. The synthetic ties for each of the three wells are consistent for both the original and inverted data, noting that they are using the same time-depth curves for both data. Most importantly, the majority of the extra events that appeared in the high-resolution data are also present in the synthetic traces.

In addition, this analysis has showed that the correlation coefficients of the synthetic seismograms with the high-resolution volumes are slightly lower as compared to the original seismic data. This is mainly due to the fact that higher frequency content in the reflectivity volumes introduces greater variability in the velocity. Another explanation for the decrease in correlation coefficients could be the increase in noise that may become evident with the increase in frequency content.

The wavelets were extracted at each well using the same time intervals with the correlation windows. The software used well-log information in addition to the seismic data for wavelet extraction. In theory, this could provide exact phase information at the well location. A limitation to this method is that it depends critically on a good well-to-seismic tie. The mistie from an inaccurate time-depth relationship can degrade the result.

The time response, amplitude spectrum and phase spectrum of the extracted wavelets for the original data and for the inverted data were compared side-by-side in the lower panels of Figure 4.6, 4.7 and 4.8. The wavelets extracted from the inversion data display sharper waveforms with smaller side lobes, while the amplitude spectra are broader. Notice the consistency in phase as it varies with frequency when comparing the original PSTM and the spectral inversion data. All of the extracted wavelets show that the both sets of wavelets have average zero phase.

The only concern is the extracted wavelet of well A. It is seen from Figure 4.6 that the shape of this wavelet is not satisfactory since the main lobe is wide with strong side lobes. It is also noticed that the amplitude below 40Hz is strong, but drops significantly above 40Hz. A distortion of the phase spectrum is noted at the extreme frequency ranges (below 10Hz and above 90Hz). However this phase distortion was observed in the extracted wavelet of the original data as well. The unfavorable characteristics described above might be explained by the inaccurate time-depth relation, or else by poor data quality since well A was drilled near two large-displacement normal faults.
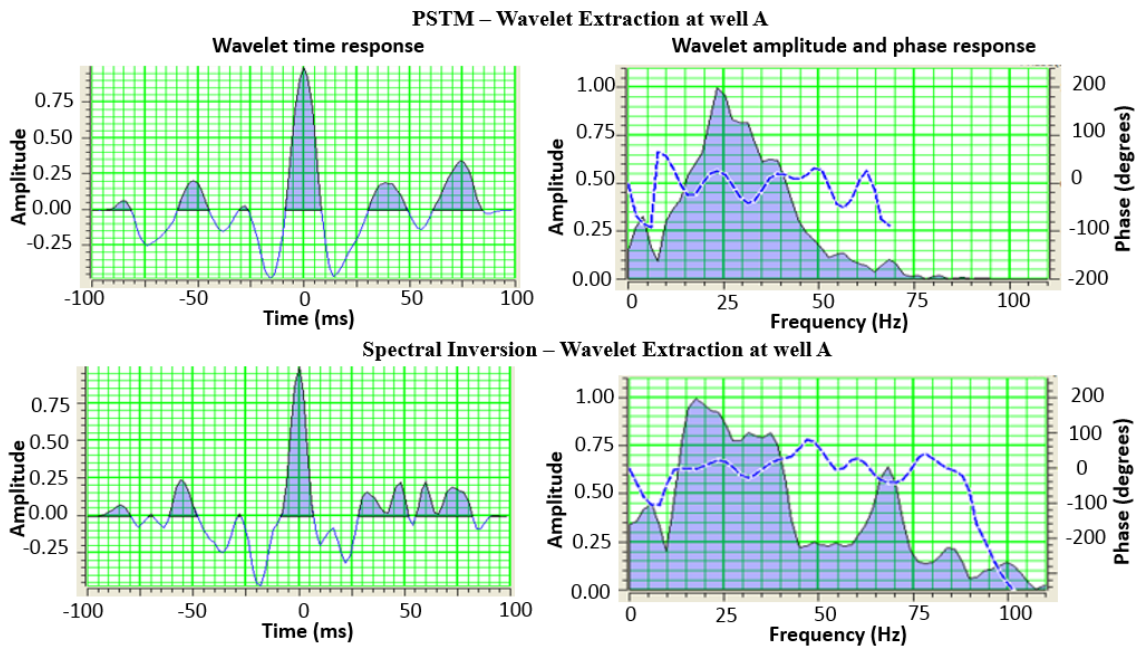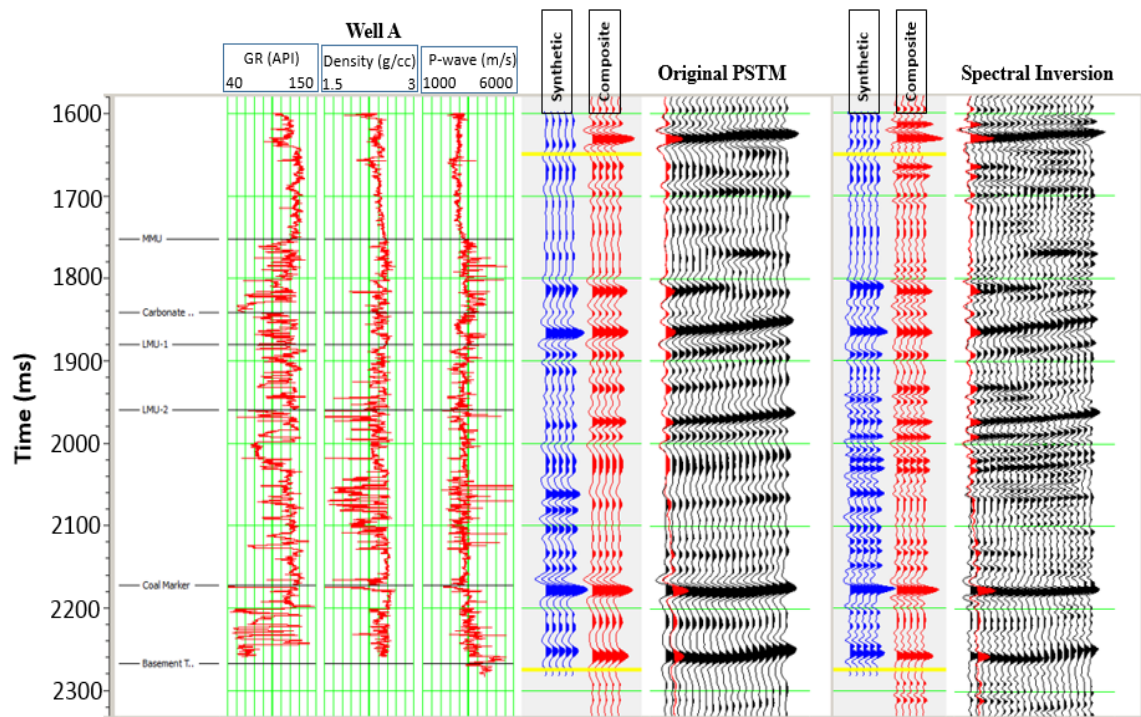
Figure 4.6: Comparison of the original PSTM data and the inversion results with their correspondent synthetic seismograms at well A. The lower panels show the wavelets extracted from each of the volumes respectively. Correlation window from 1650 ms to 2275 ms gives correlation factors of 0.73 for the original data and 0.68 for the inversion data.
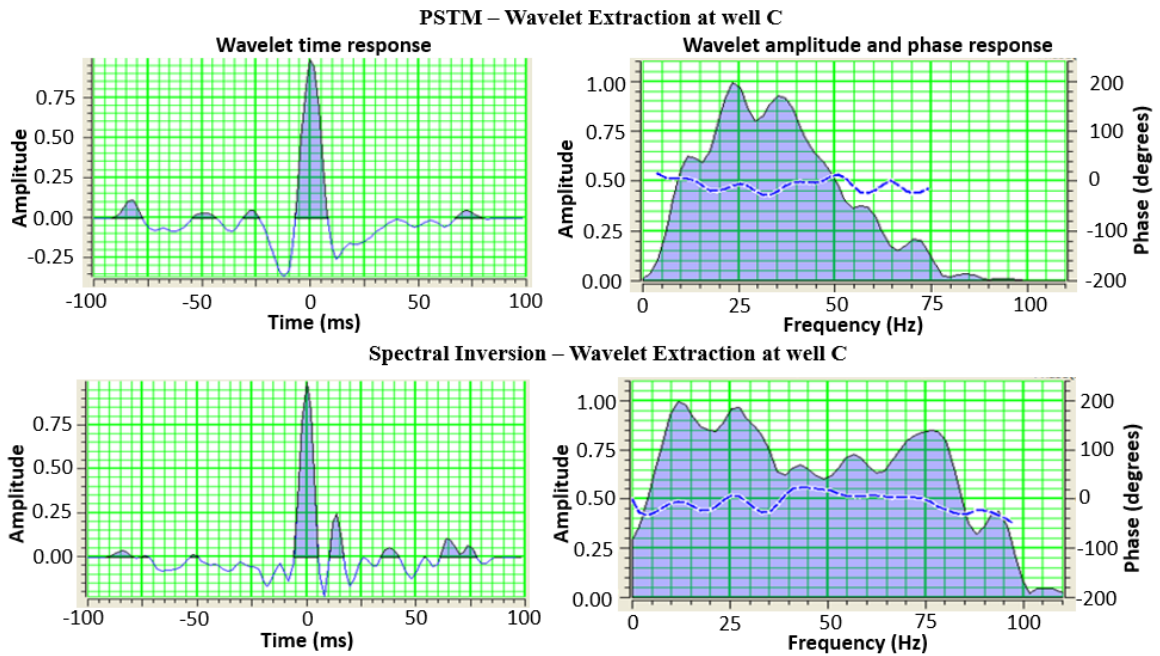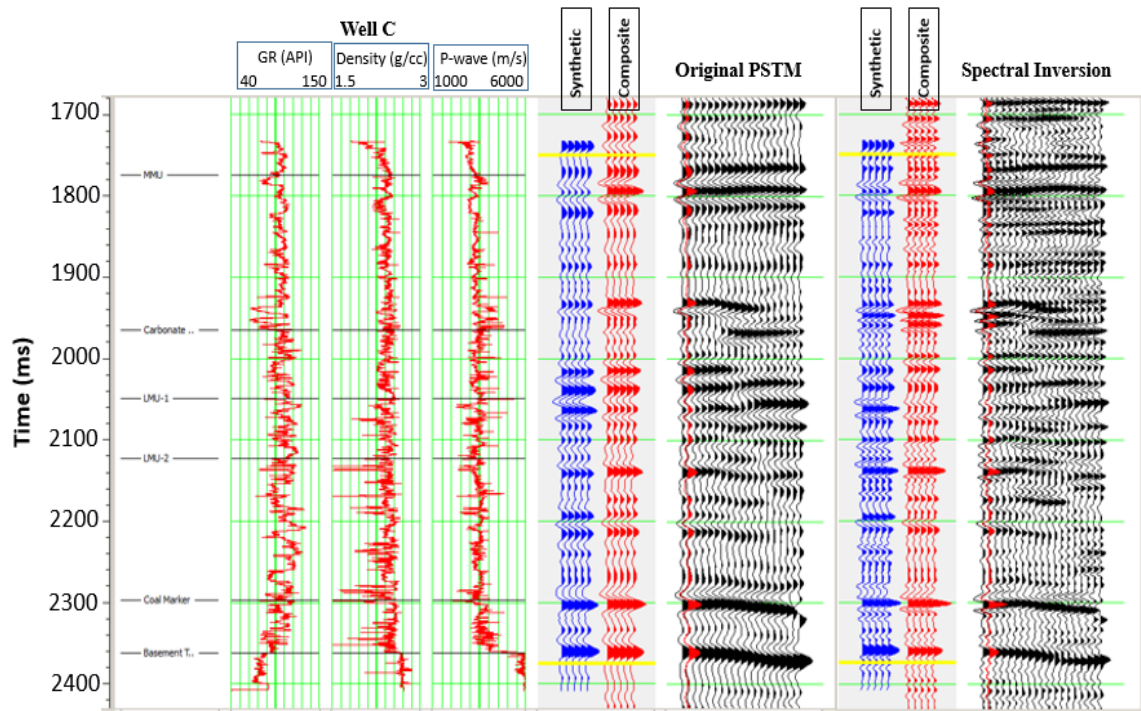
Figure 4.7: Comparison of the original PSTM data and the inversion results with their correspondent synthetic seismograms at well C. The lower panels show the wavelets extracted from each of the volumes respectively. Correlation window from 1750 ms to 2375 ms gives correlation factors of 0.83 for the original data and 0.76 for the inversion data.
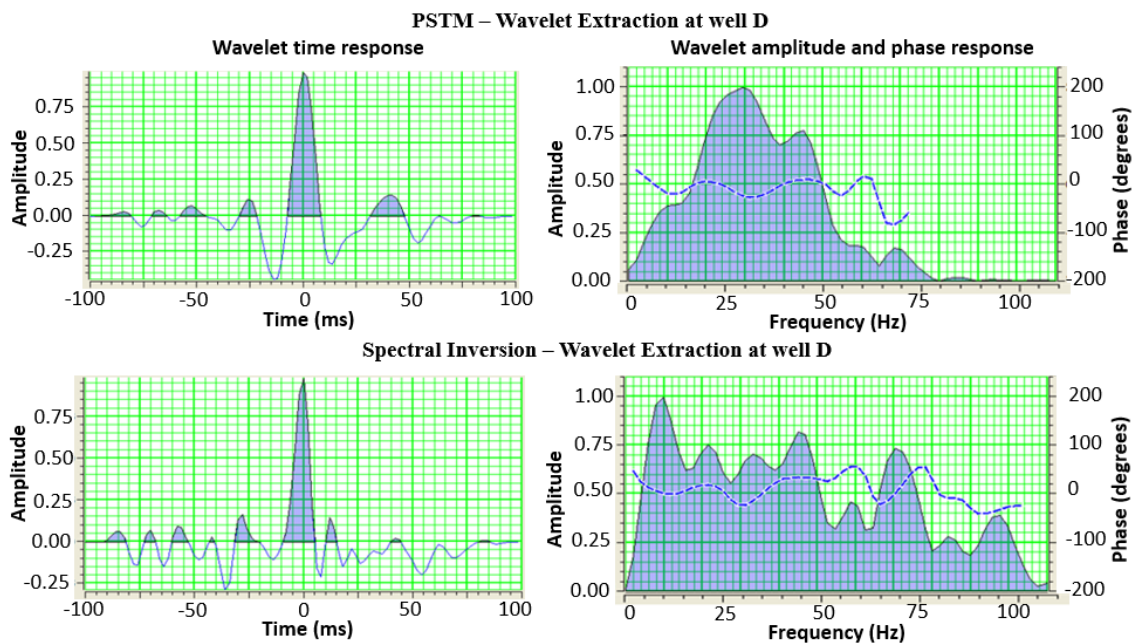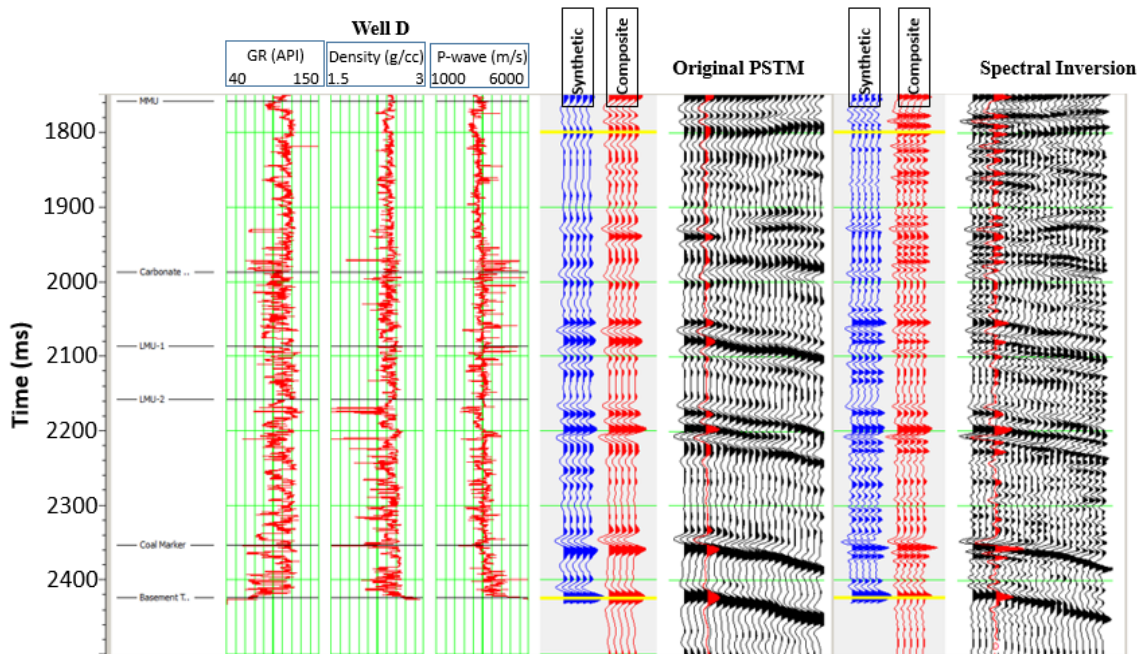
41

Figure 4.8: Comparison of the original PSTM data and the inversion results with their correspondent synthetic seismograms at well D. The lower panels show the wavelets extracted from each of the volumes respectively. Correlation window from 1800 ms to 2425 ms gives correlation factors of 0.81 for the original data and 0.74 for the inversion data.

4.2 Wavelet Deconvolution Results

Wavelet deconvolution is a deterministic method which use the wavelets extracted from seismic data to remove the effect of the wavelet and to bring the reflections closer to the Earth reflectivity. In this study wavelet deconvolution was attempted in order to improve the vertical resolution slightly and provide higher resolution data for interpretation.

Several wavelet deconvolution tests were performed in Hampson Russell using a range of different wavelets. Wavelet deconvolution workflows allow the use of a single wavelet, an average wavelet or a group of wavelets. Other parameters include the operator length and pre-whitening level. Theoretically, as the length of the operator is increased, we assume greater complexity in the seismic wavelet, and get a more pronounced or harsh deconvolution effect. However, the enthusiasm to increase operator length must be balanced against its tendency to increase the high-frequency noise level. Because the spectral inversion data are already high-resolution with flat spectrum, an operator length of 60 ms and a pre-whitening of 2 % were chosen, resulting in a deconvolution effect that was within acceptable limits. The wavelet deconvolution was an optional step in this study and was intended to produce minor improvement to the data before interpretation.

The previous section described how our efforts to correlate data from wells C and D with spectral inverted data yielded very acceptable ties with high correlation factors of 0.76 and 0.74 respectively. In addition, the extracted wavelets for wells C and D displayed good characteristics in the time domain along with stable amplitude spectra.

Therefore, the average wavelet obtained from wells C and D (Figure 4.9) was used to generate the final version of the wavelet deconvolution that produced the most stable results, the best well-tie and the best overall wavelet characteristics.
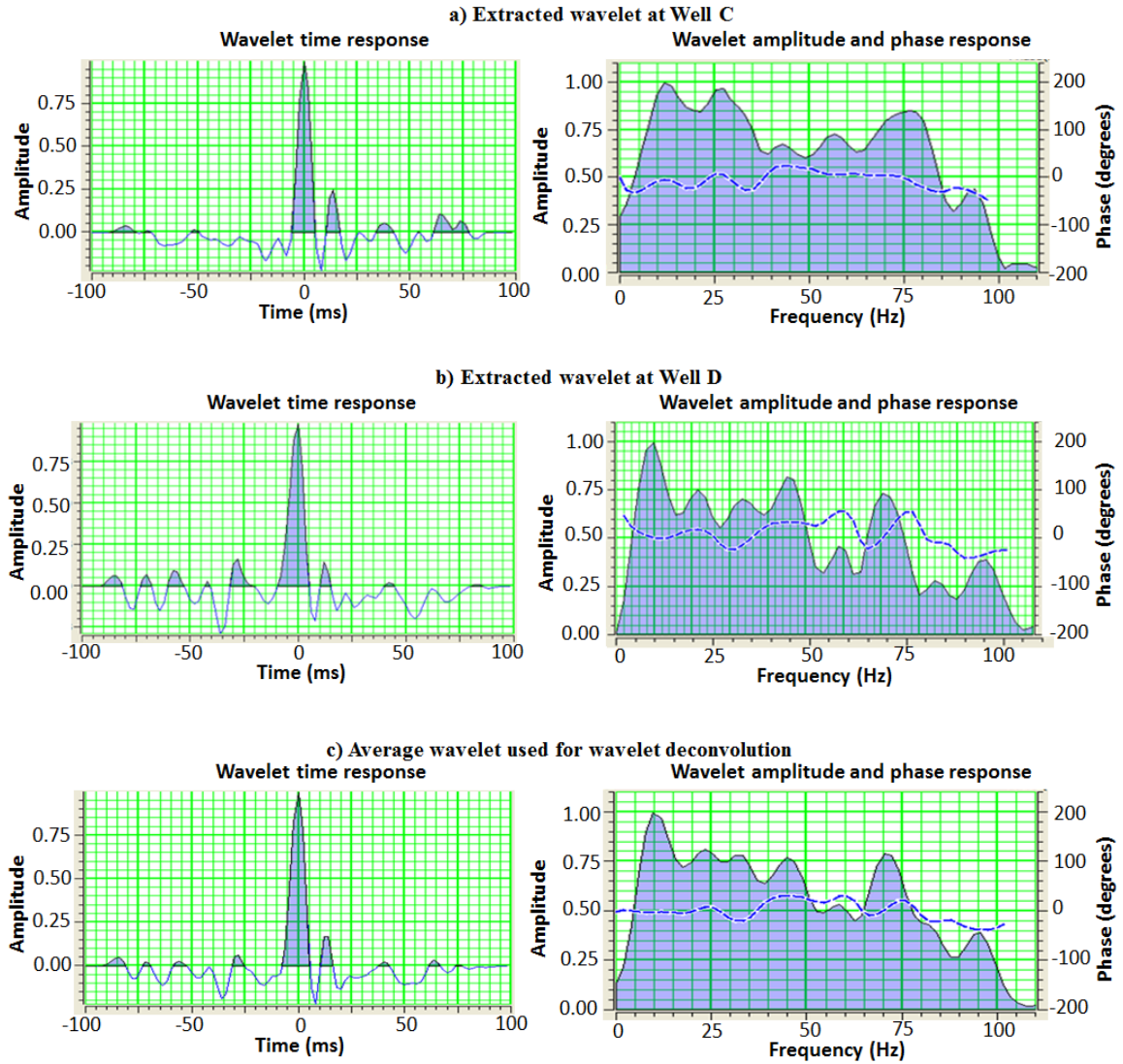

Figure 4.9: Wavelet time responses (left panels) and amplitude and phase spectra (right panels) for a) extracted wavelet at well C, b) extracted wavelet at well D, c) average wavelet used for wavelet deconvolution. Phase spectra are represented by dashed line.

Figure 4.10, 4.11 and 4.12 show the spectra of single traces extracted from the spectral inversion data at the respective well locations before and after wavelet deconvolution and compare them with the well reflectivity spectra. It is seen that the spectrum of a reflectivity series generated from actual well logs is close to the blue spectrum instead of the assumed white spectrum. Because the actual well logs are available only in a short window, the spectrum of a reflectivity series is far from an ideal white spectrum due to the inadequacy of the statistics (Guofa, 2009).
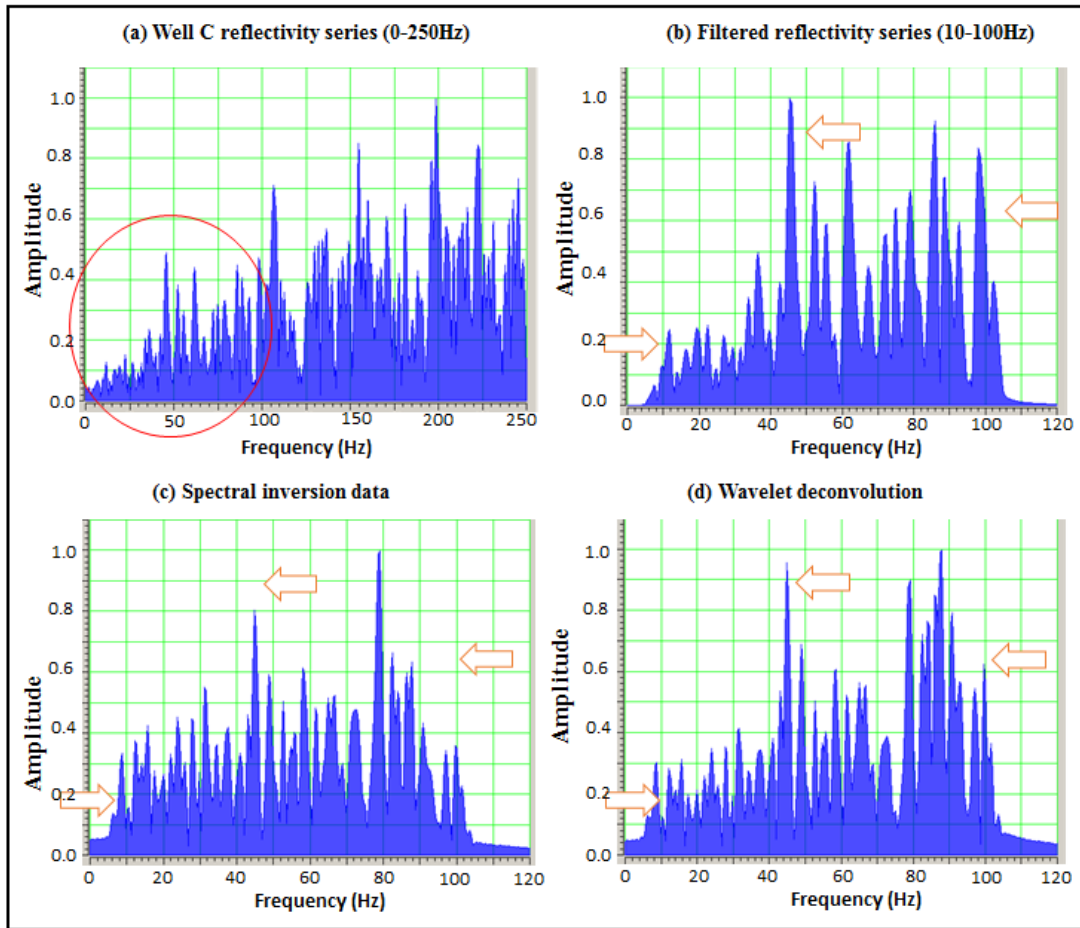

Figure 4.10: Amplitude spectra of a) well C reflectivity series b) filtered reflectivity series (10-100 Hz) c) spectral inversion data and d) wavelet deconvolution data. The spectrum after wavelet deconvolution (d) yields better match with the reflectivity spectrum derived from the well data (b).
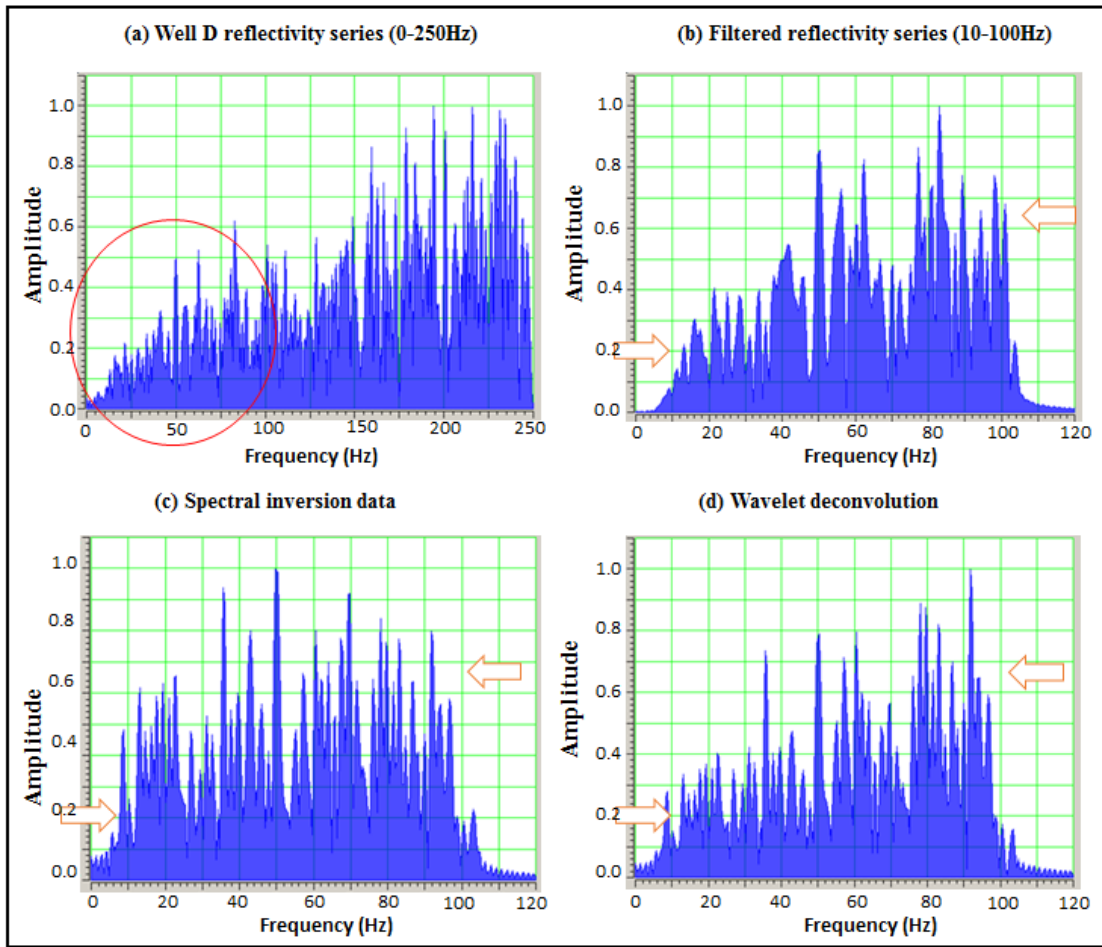
Figure 4.11: Amplitude spectra of a) well D reflectivity series b) filtered reflectivity series (10-100 Hz) c) spectral inversion data and d) wavelet deconvolution data. The spectrum after wavelet deconvolution (d) yields better match with the reflectivity spectrum derived from the well data (b).
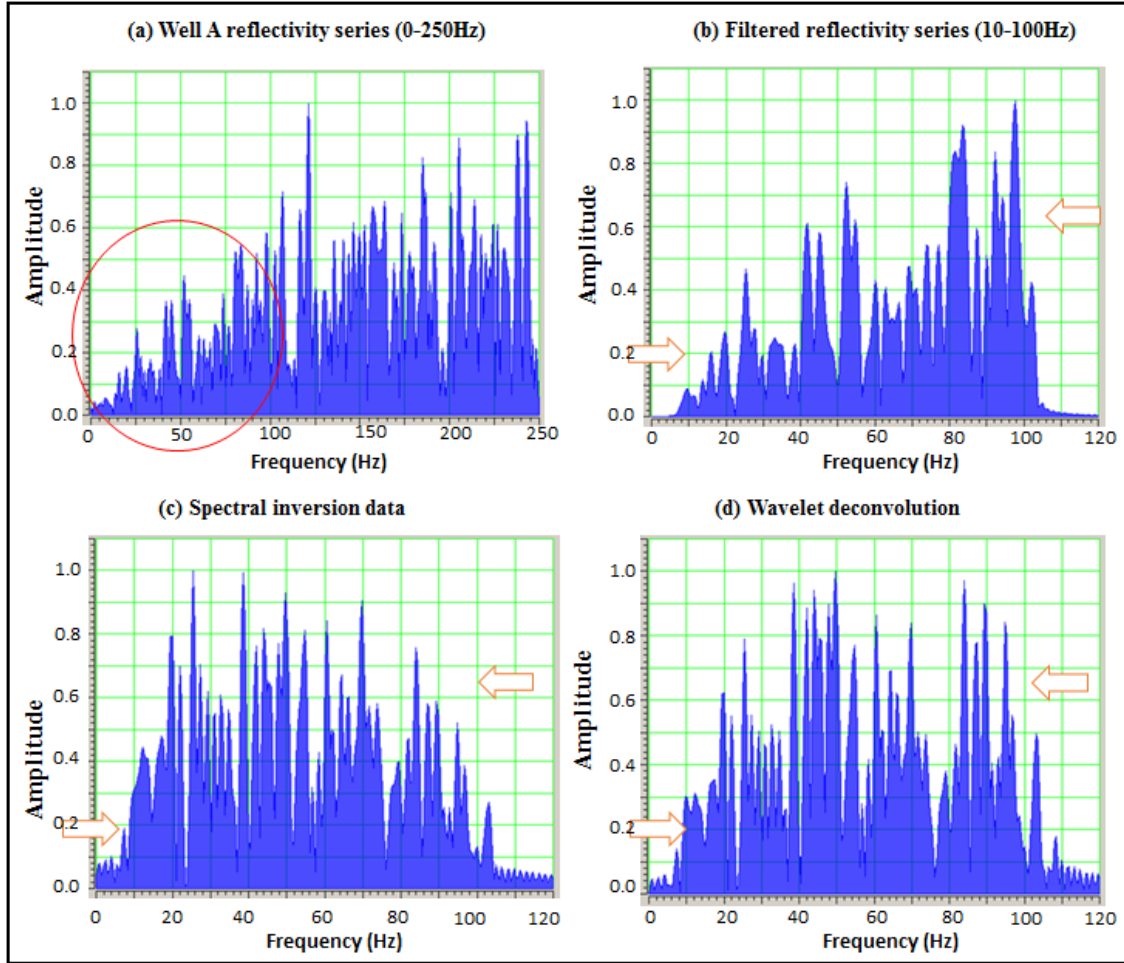
Figure 4.12: Amplitude spectra of a) well A reflectivity series b) filtered reflectivity series (10-100 Hz) c) spectral inversion data and d) wavelet deconvolution data. The spectrum after wavelet deconvolution (d) yields better match with the reflectivity spectrum derived from the well data (b).

In general, the wavelet deconvolution depressed the amplitude of the low frequency content while slightly increased the amplitude of the high-frequency content. According to three figures above, the amplitude spectrum of the high-resolution data after wavelet deconvolution has deviated from white spectrum (flat) but shows a better match with the reflectivity spectrum derived from well log, and this indicates that the resulting reflections from wavelet deconvolution process are closer to the true earth reflectivity.

To illustrate the improvement after deconvolution, three seismic sections are shown in Figure 4.13. The data after wavelet deconvolution yield a slight improvement in vertical resolution and the lateral continuity, which makes the interpretation of high-resolution data more efficient.
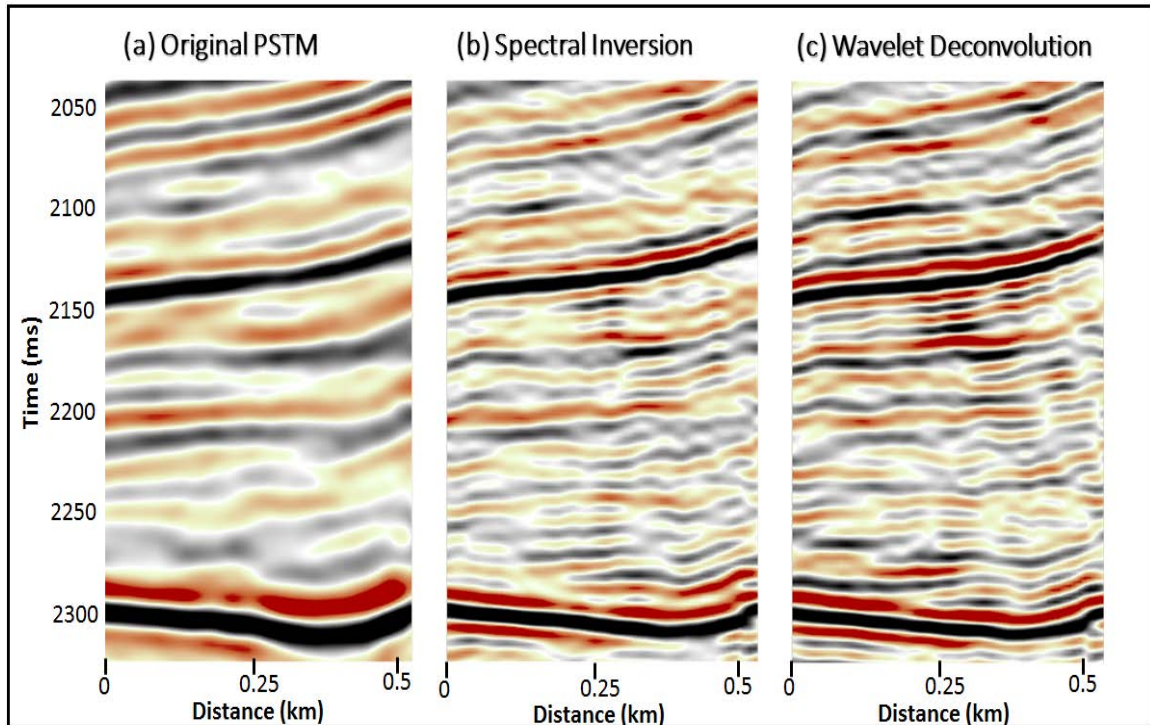

Figure 4.13. Seismic sections of (a) original PSTM data (b) spectral inversion data (c) after wavelet deconvolution. The data resulted from wavelet deconvolution show more continuous events and minor resolution improvement compared to spectral inversion data. Peaks (positive amplitude) are black; troughs (negative amplitude) are red.

Comparison of the extracted wavelets after the wavelet deconvolution process illustrates improvement (Figure 4.14). The time response of the wavelet more closely resembled a spike while high frequencies were recovered as seen in the amplitude spectra of the wavelets. An important point to note is that the phase spectra remain almost unchanged throughout the process.
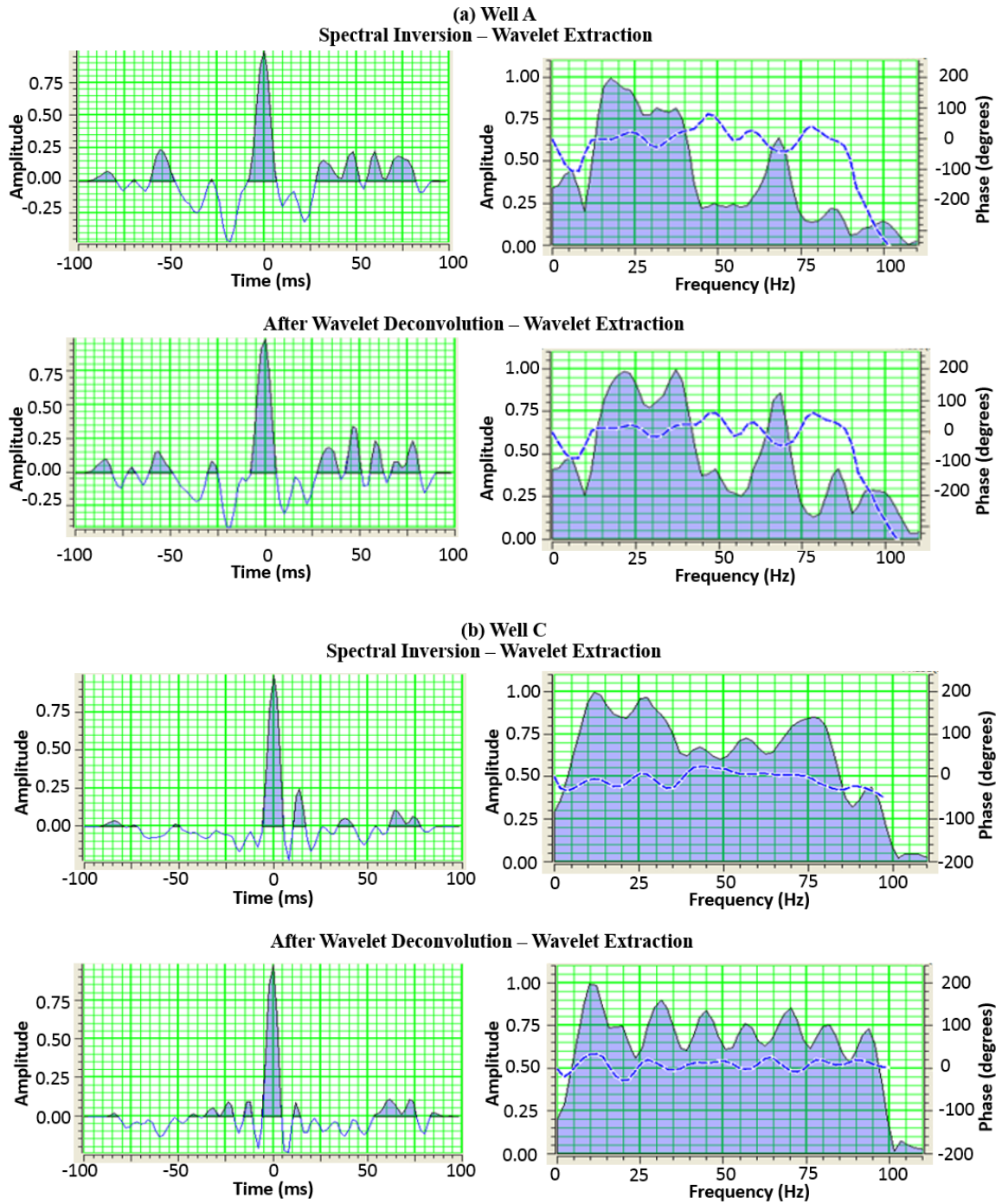
48

Figure 4.14: Comparison of extracted wavelets from spectral inversion data and wavelet deconvolution data for a) well A b) well C
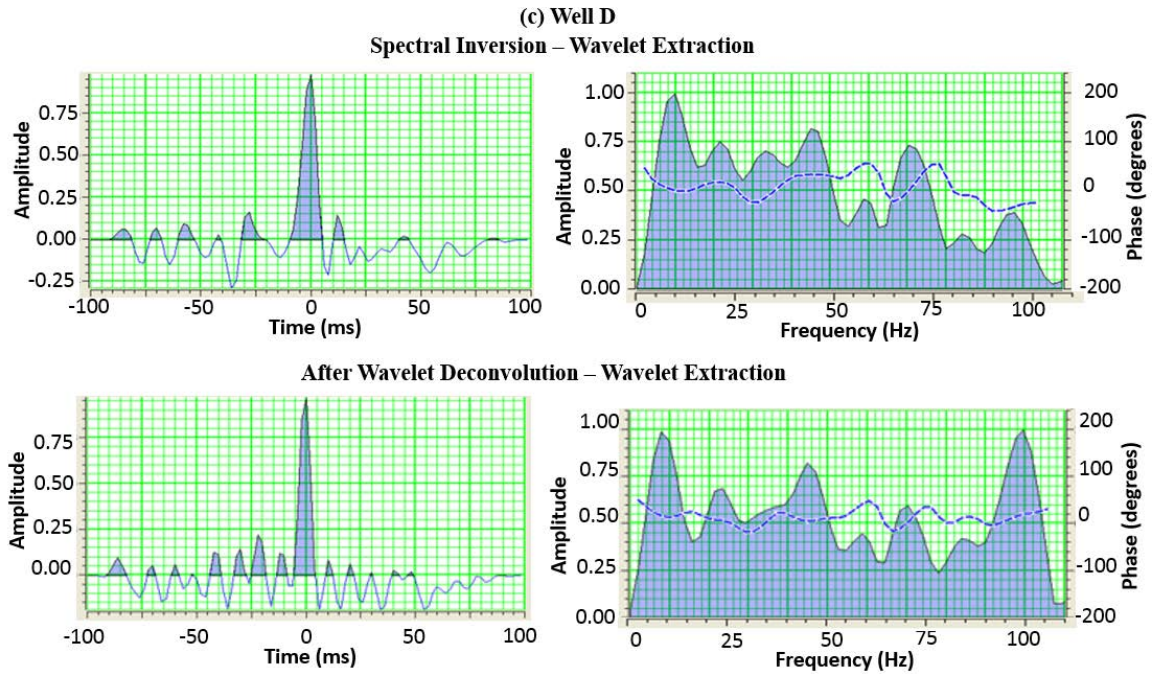
(c) Well D
Spectral Inversion – Wavelet Extraction

After Wavelet Deconvolution – Wavelet Extraction

Figure 4.14 (cont): Comparison of extracted wavelets from spectral inversion data and wavelet deconvolution data for c) well D

Resolution Improvement

To quantify the improvement in vertical resolution, the average bandwidth and calculated resolution for three dataset are shown in Table 4.1. The process of spectral inversion almost doubled the original frequency content and provided superior vertical resolution, while wavelet deconvolution helped to slightly increase resolution. The average velocity within the reservoir level is 3386 m/s, which results in average vertical resolution limits of 28 m, 15.4 m and 13.1 m for the original data, spectral inversion data and the result of wavelet deconvolution respectively.
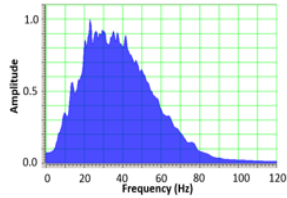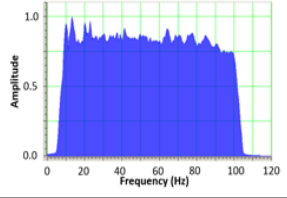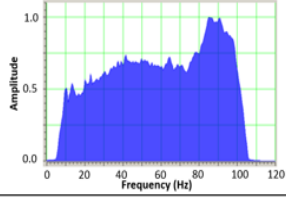
Average Amplitude spectrum (Amplitude vs Frequency)	(Average velocity = 3386m/s)	Frequency Bandwidth (Hz)	Average Frequency (Hz)	Calculated Depth resolution (m) = 1/4* v/f	Calculated TWT Resolution (ms)
	PSTM	20-65	~ 33	~ 25 m	~ 15 ms
	Spectral Inversion	10-100	~ 55	~15 m	~ 9 ms
	Wavelet Deconvolution	10-100	~ 65	~ 13 m	~ 7.5 ms

Table 4.1: Comparison of bandwidth and resolution improvement: (top) original PSTM, (middle) Spectral Inversion and (bottom) after Wavelet Deconvolution. Spectral inversion broadened the bandwidth and improved resolution significantly.

The improvements in resolution are illustrated in Figure 4.15, in which seismic sections displaying the spectral inversion data before and after wavelet deconvolution both show more reflections than the original seismic data, which tie with synthetic traces. Notice how the interference effects at the top and base of Sand 1 were better resolved with the high-frequency data. Sand 1 is well defined on the gamma ray (GR) log and a distinct thin coal layer is present at its base. Even though the thickness of Sand 1 at well A (32.5 m) is above the average resolution of the original data, the base is not resolved due to an interference effect with the thin coal layer. On high-resolution data, the top and base of Sand 1 can be interpreted independently.
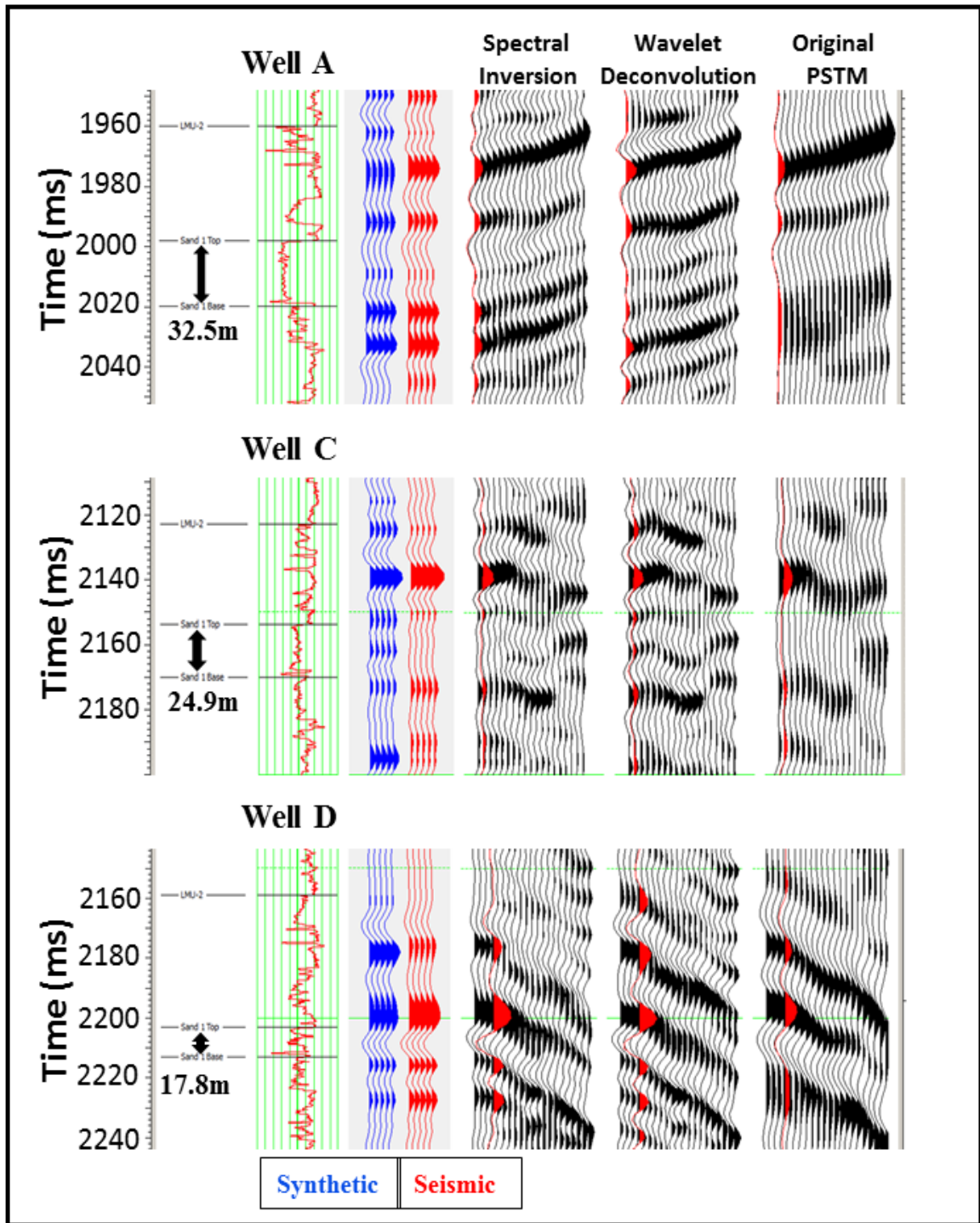
51

Figure 4.15: Well-ties comparison of three wells with original PSTM data, spectral inversion data, and wavelet deconvolution data. High-resolution data that resulted from spectral inversion and wavelet deconvolution are able to resolve the wavelet interference patterns at top and base of Sand 1.

52

5. ENHANCED SEISMIC INTERPRETATION

With broader frequency bandwidth, the seismic data obtained from the spectral inversion improved the vertical resolution and revealed more layers than the normal frequency data. As a result, structural and stratigraphic interpretation can be performed with higher accuracy.

5.1. Improvements in stratigraphic interpretation

Figure 5.1 and 5.2 display two examples of stratigraphic features visible in the original seismic data and the high-resolution data. The carbonate platform, which is a distinct geological feature in this area, looks very different in the two data sets. On the original seismic data, an apparent discontinuity can be seen at about 1970 ms. The discontinuity might be interpreted as a localized fault or as a stratigraphic discontinuity in layering within the carbonate platform. However, the inverted data shows a different picture of the layering. The high-resolution data reveal more layers with greater detail and, perhaps most importantly, the apparent discontinuity in layering does not appear in the inverted section. Compared to the adjacent well and the stratigraphic sequence above and below the carbonate platform, the image observed in the high-resolution data makes more geological sense. The apparent discontinuity might be explained as a result of destructive wavelet interference in the original seismic data.
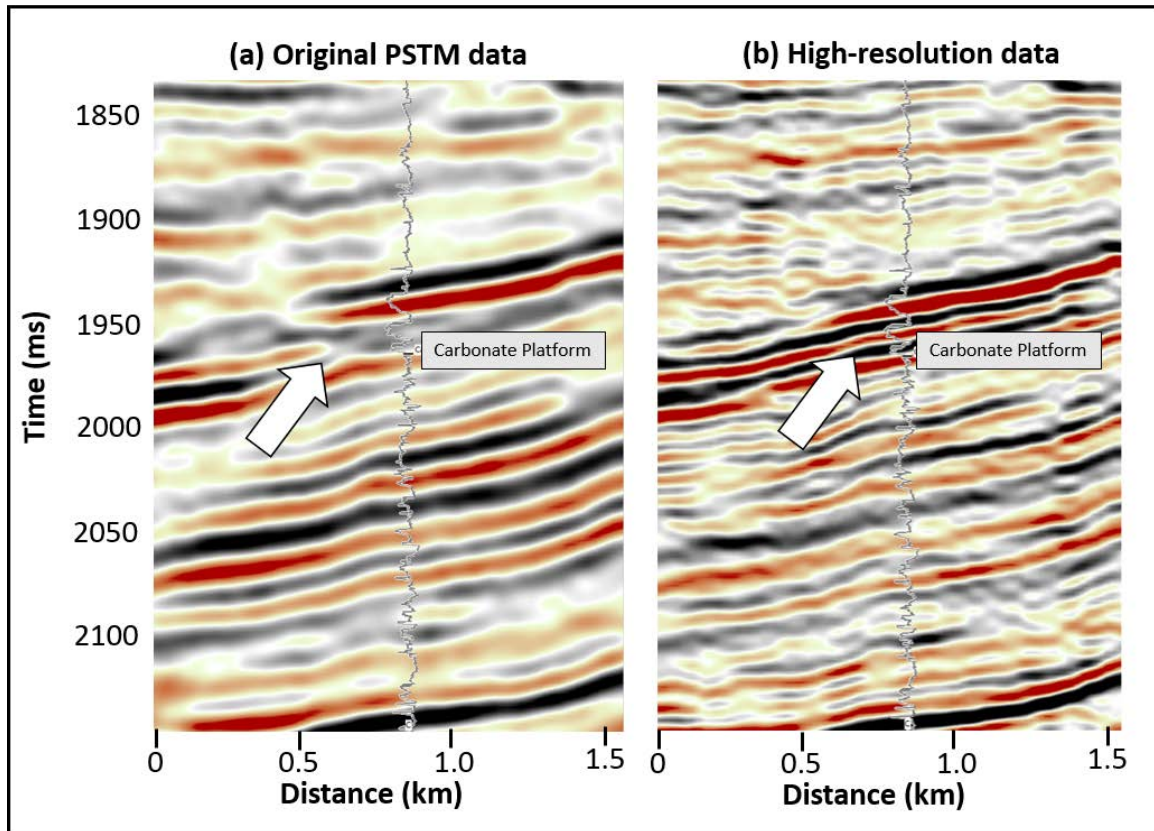
Figure 5.1: Comparison of the original PSTM data and high-resolution data. (a) Original seismic data shows a discontinuity. (b) The inverted data reveals continuous layering, suggesting the discontinuity in (a) is actually a wavelet effect rather than a real geological feature. Peaks (positive amplitude) are black; troughs (negative amplitude) are red.
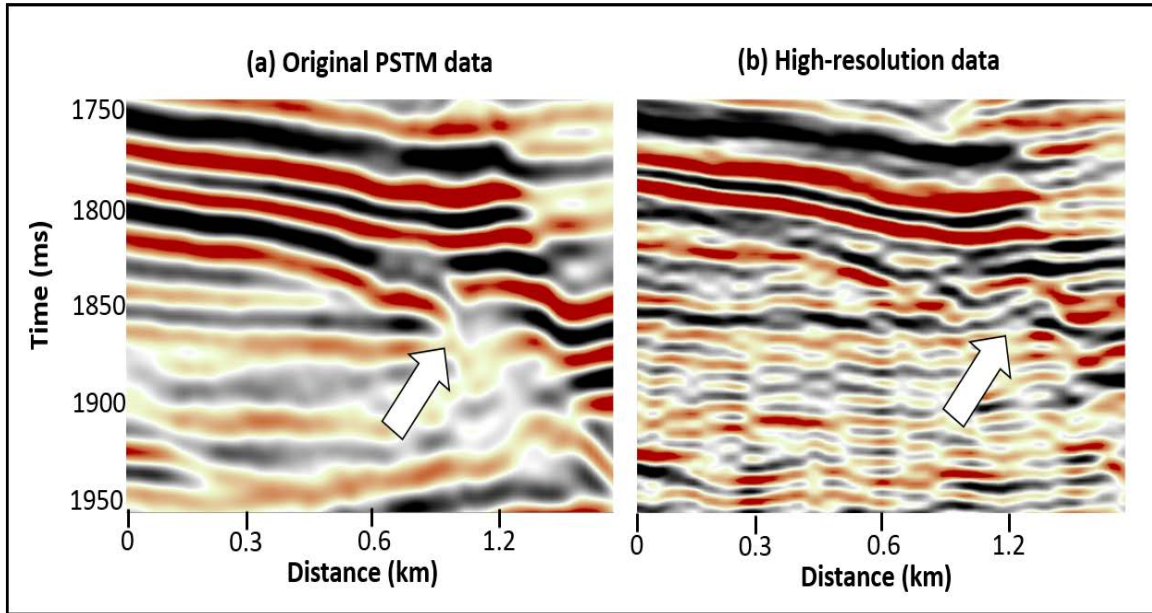
Figure 5.2: (a) The original seismic profile shows an apparent discontinuity, while (b) the high-resolution data reveals as continuous event which might be interpreted as a maximum flooding surface. Peaks (positive amplitude) are black; troughs (negative amplitude) are red.

Another example of the apparent discontinuity is shown in Figure 5.2. The high-resolution seismic section displays a continuous event interpreted as a possible maximum flooding surface, over which exists a down-lapping stratigraphic sequence. The discontinuous events on the original data are actually not geologic features but geophysical effects, caused by the wavelet overprints.

An important point is that this inversion method does not require initial model from well data. It only requires the seismic data input; therefore it has no horizons or lateral continuity constraints. The lateral continuity that is observed is a good indication of the robustness and stability of the inversion algorithm.

Previously described in the stratigraphic section, the reservoirs in this area are stacked sands inter-bedded with claystones and thin coal layers. This characteristic results in a

55

complex reflectivity pattern, which creates wavelet interference at the top and bottom of the sand reservoirs. One of the sand beds, label Sand 1, which has a varying thickness throughout the field, was not resolved completely in the original PSTM data. However top and base of Sand 1 were able to be mapped on the high-resolution data.

Figure 5.3 and 5.4 show two seismic profiles though well A and C on which the top and bottom of Sand 1 are correlated and were tied back to their picks on the GR log. On the inversion volume (right panel), distinct reflections appear at the top and base of the bed in each well. The top of the sand can be correlated with a trough (red) and the bottom was picked on the peak (black).

Figure 5.3: A seismic section through well A. Notice the top and base of sand 1 are resolved on the high-resolution data. Top of Sand 1 corresponds to a trough (red) and base of Sand 1 corresponds to a peak (black). Thickness of Sand 1 in this well is 32.5 m. Peaks (positive amplitude) are black; troughs (negative amplitude) are red.
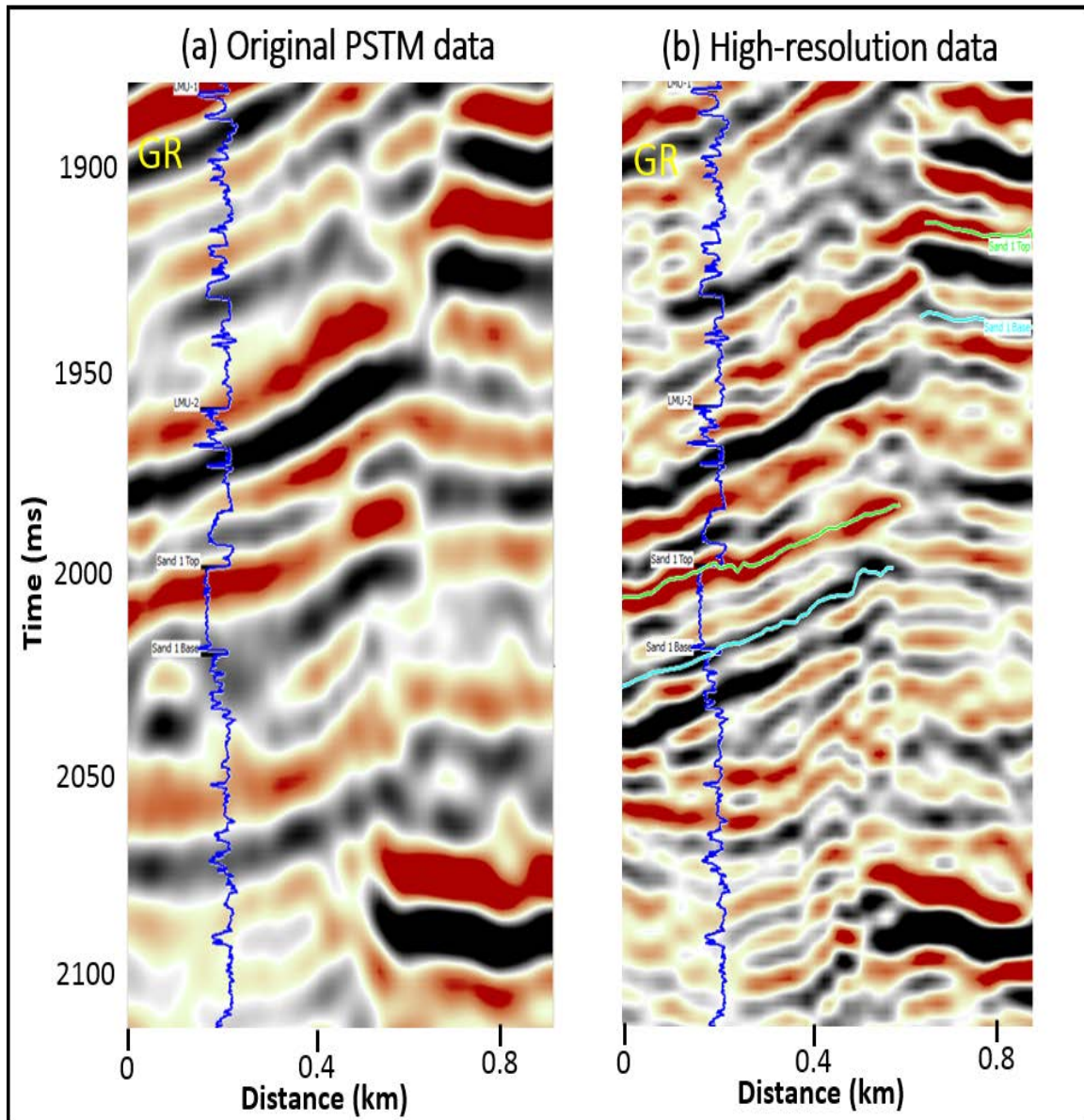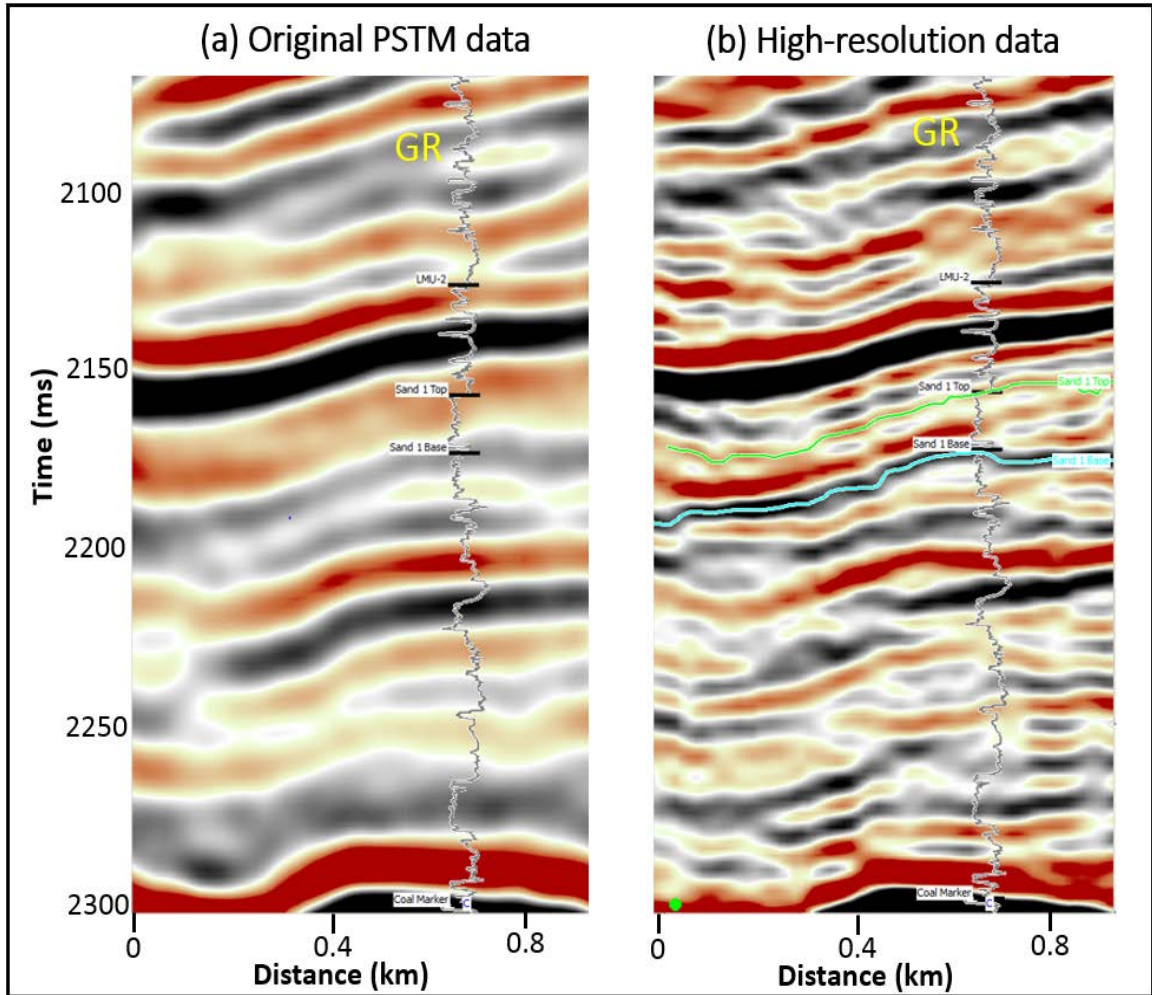
Figure 5.4: A seismic section through well A. Notice the top and base of sand 1 are resolved on the high-resolution data. Top of Sand 1 corresponds to a trough (red) and base of Sand 1 corresponds to a peak (black). Thickness of Sand 1 in this well is 24.88 m. Peaks (positive amplitude) are black; troughs (negative amplitude) are red.

The southern part of the survey is strongly faulted with apparent lower signal to noise ratio as compared to the other areas. As can be seen in Figure 5.5, the structure is broken by a complex series of normal faults. The unfavorable characteristics of the input partially affected the results of spectral inversion. The top and bottom of Sand 1 were not interpretable in this area, thus not being shown on the maps below.
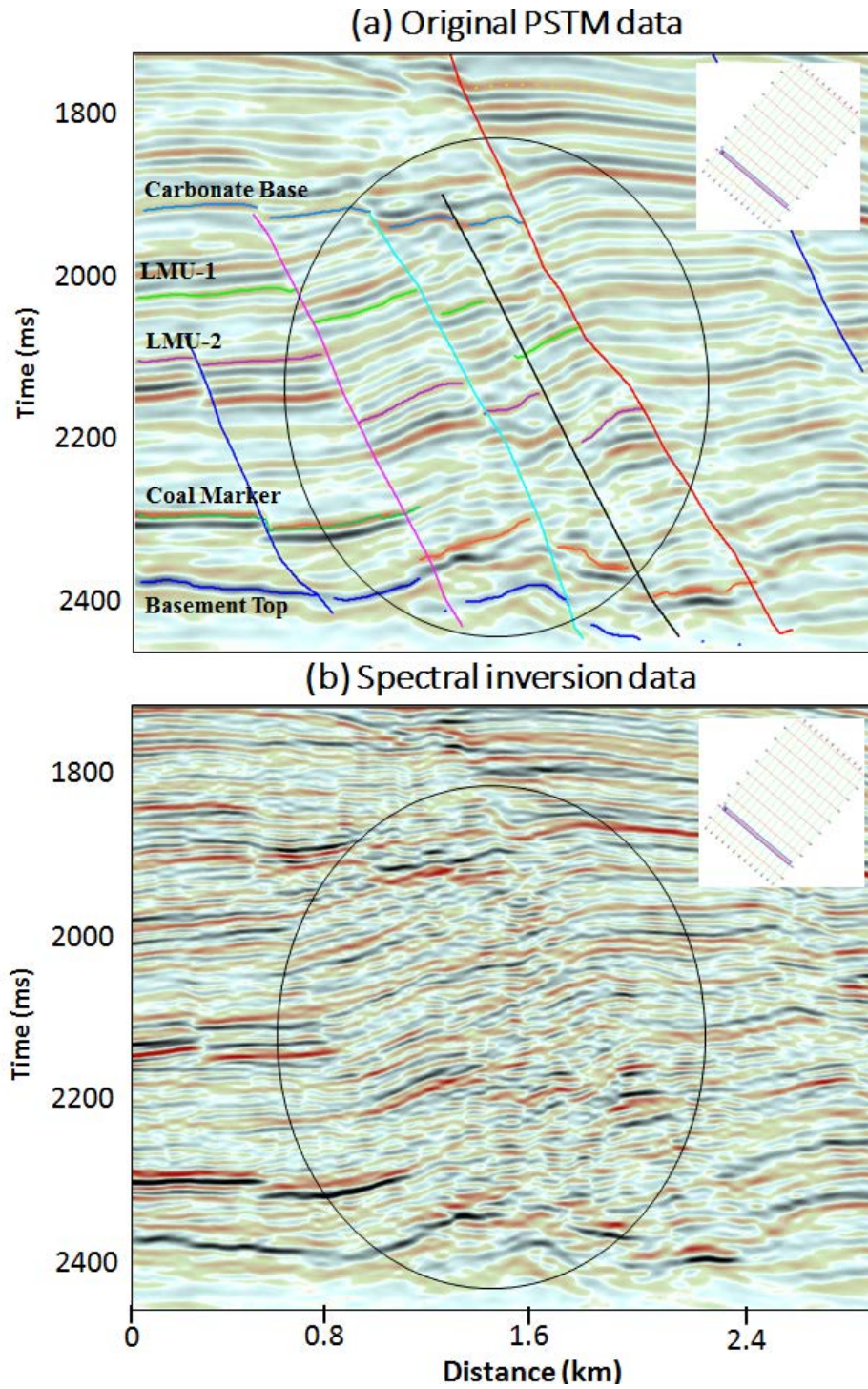
58

Figure 5.5: Seismic sections of (a) Original data and (b) high-resolution data. Horizon and fault interpretation are displayed on the original data. The complex geology and low signal to noise ratio of the input data partially affected the spectral inversion result. Peaks (positive amplitude) are black; troughs (negative amplitude) are red.
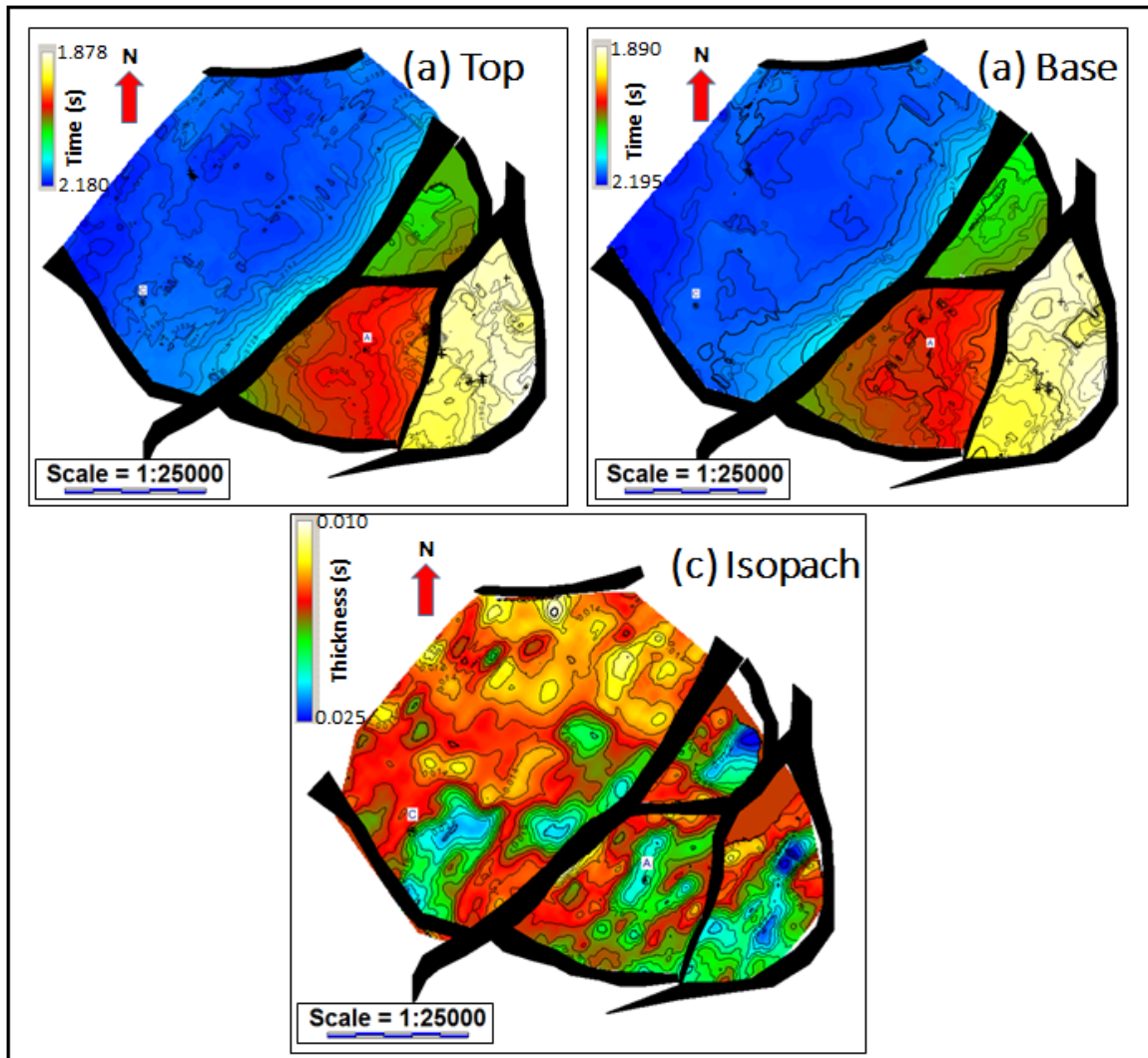
Figure 5.6: Time-structure maps for a) top and b) base of Sand 1; c) Sand 1 isopach map

The time-structure maps for the top and bottom of Sand 1 that were interpreted on the

high-resolution seismic volume are shown in Figure 5.6 (a & b). It is not possible to pick

the top and base of this sand formation on the original seismic data, limiting the direct

comparison with the picks on high-resolution data. The isopach map of Sand 1 (Figure

5.6, c) shows a good correlation between the apparent time thickness obtained from map

and the thickness obtained from well logs, which again confirms the well-ties and lateral

stability of the high-resolution data. The isopach map also illustrates a trend in an east-west direction where the sand is thicker than it is to the northeast. This trend could represent a stratigraphic features related to the depositional environment of the sand reservoir.

5.2 Improvements in structural interpretation

Previously discussed in the section of geological settings, there is a great deal of faulting in this area and which has resulted in severe internal compartmentalization of the reservoirs, which in turn require the most detailed and accurate fault mapping that can be obtained. Not only are the major faults that define the structure framework important, the small-throw faults with 20 m of displacement or less are also important as they may control the effectiveness of the fault seals that are critical for trap definition.

Analysis of time slices provides a general idea basis for fault identification and mapping. Figure 5.7 shows a time slice from both the original seismic and the high-resolution data at 1926 ms. The high-resolution data reveal more minor faults in the central block that could not be resolved in the original data.
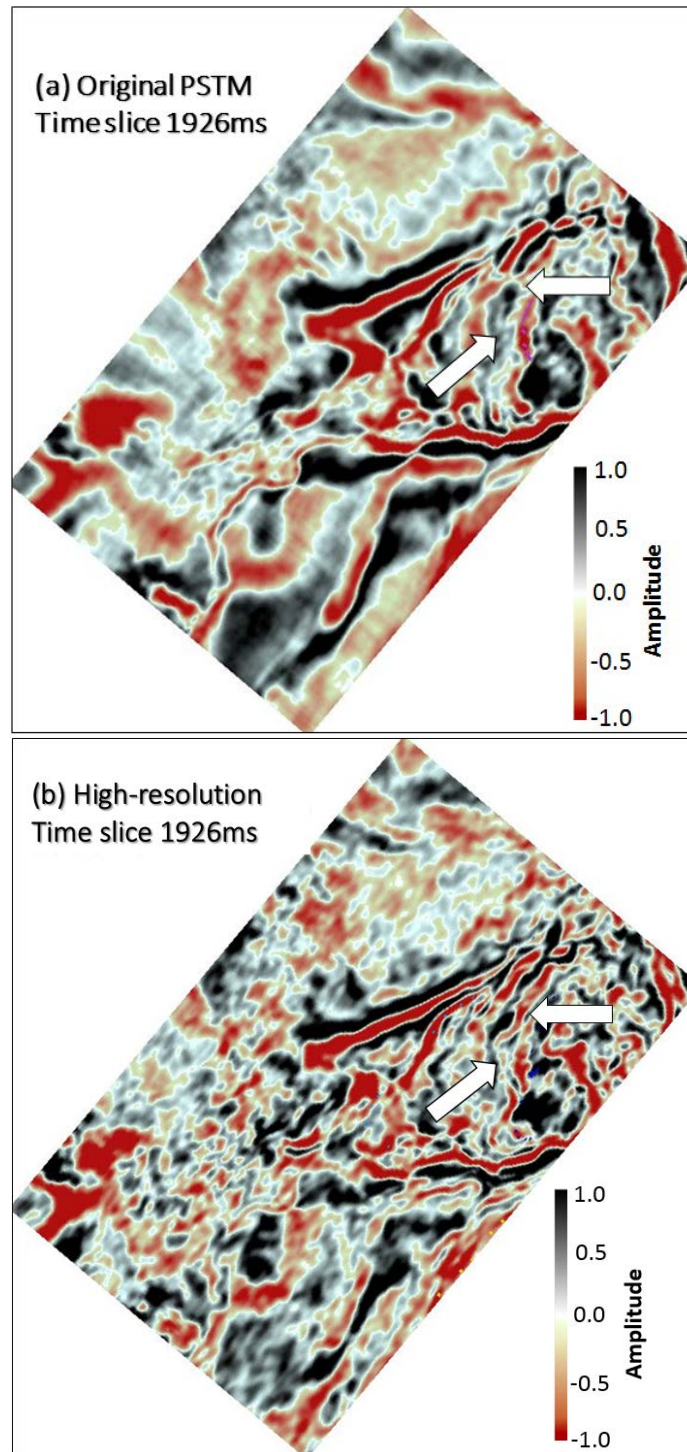
Figure 5.7: Time slice at 1926 ms for (a) original PSTM data and (b) high-resolution data. Minor faults are revealed in the high-resolution data (arrow). Positive amplitude is black; negative amplitude is red.
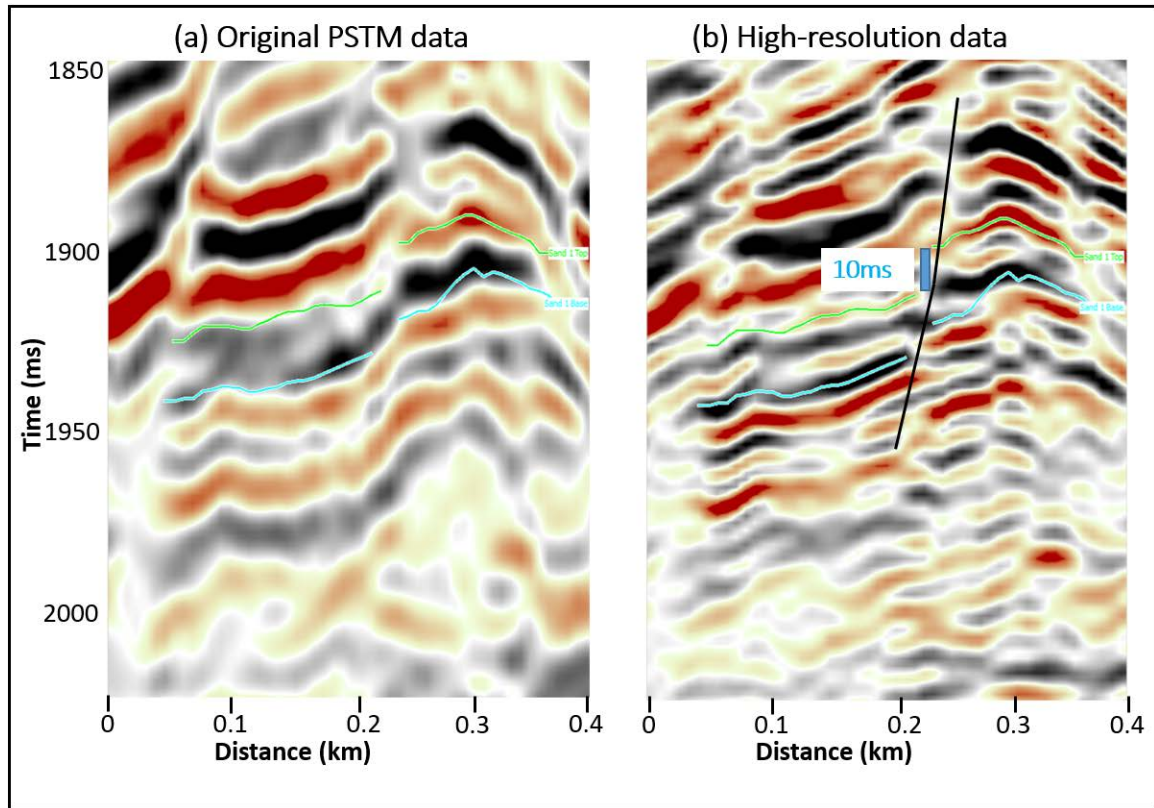
Figure 5.8: A cross section showing a small displacement fault revealed on the high-resolution data (b) which were not seen on the original seismic (a). Fault displacement is approximately 10 ms in time or 16 m in depth. Peaks (positive amplitude) are black; troughs (negative amplitude) are red.

A seismic section cutting through the central block (Figure 5.8) supports the observations of improvement fault recognition with the high-resolution seismic data that were seen on previous time slices. The central area shows an anticlinal feature in the original seismic; however in the high-resolution data small-throw faults are resolved. These beds are not just folded, but are broken up by the minor faults with throw of approximately 16 m. These features could affect the continuity of the sand beds, which could in turn lead to problems in fluid flow.

6. CONCLUSIONS

The results of this study show that the spectral inversion process can be applied to conventional seismic data to extend the frequency bandwidth and increase resolution. In this study the frequency content of the PSTM seismic data was broadened from 20-65 Hz to 10-100 Hz, resulted in improving vertical resolution from 28 m to 15.4 m.

The inverted data are generally stable in the whole test area and provide superior vertical resolution than the original PSTM data. Well log correlations for both the input and the inversion results show reasonable correlation coefficients, which confirm the validity of the increased frequency content. Wavelet deconvolution was applied as an optional step to the inversion data to marginally enhance the inverted data, thus increasing the resolution to 13 m and bringing the seismic traces closer to the actual earth reflectivity.

Comparison of synthetic well-ties and key seismic profiles has shown that the interferences effects of the sand reservoirs with inter-bedded claystones and thin coal layers were well-resolved. The improvement in resolution has permitted a better identification of individual sand formation tops and bases. Thus, an understanding of the distribution of reservoir sand package has been enhanced. Additional top and base of sand bodies were interpreted throughout the area with good lateral continuity. Several stratigraphic examples illustrate that some apparent discontinuities in the original seismic data were revealed as continuous features by the inversion process. The spectral inversion was performed trace by trace, with no initial model for continuity constraints. Therefore, such continuity can be explained as being due to actual geological continuity masked by

the seismic wavelet. The lateral continuity of the newly picked horizon serves as an additional indication of the stability and robustness of the method. The high-resolution data also revealed several small-throw faults with displacement of 16 m in the central block which are not obvious in the original seismic data. This information gives valuable contribution to the delineation of individual sand bodies and their connectivity.

   In the southern area where there exists a complexly-faulted structure within an area of lower signal to noise ratio, the inversion results were less successful, as the increase in frequency content of the data also boosted the noise. However, presence of noise can limit the results of any seismic inversion method, not only the spectral inversion. These results clearly show that spectral inversion is a very useful tool in hydrocarbon exploration. Using denser well information together with production data could provide more detailed verification of the spectral inversion technique.

REFERENCES

Bat, D., H. Quynh, P. H. Que, and T. L. Dong, Tertiary stratigraphy of continental shelf of Vietnam, *in* First International Seminar on the Stratigraphy of the Southern Continental Shelf of Vietnam, Hanoi, January 14-17, 1993, unpaginated.

Brown, A., 1999, Interpretation of Three-dimensional Seismic Data: SEG/AAPG, SEG Investigations in Geophysics #9, 6th Edition, 560 pp.

Castagna, J.P., S.J.Sun, 2003, Instantaneous spectral analysis: Detection of low - frequency shadows associated with hydrocarbons: The Leading Edge 120 - 127.

Castagna, J. P., 2005, Spectral decomposition and high-resolution reflectivity inversion: Presented at CSEG National Convention,

Castagna, J. P., and S. Sun, 2006, Comparison of spectral decomposition methods: First Break, EAGE, 24, 75-79.

Chakraborty, A., D. Okaya, 1995, Frequency- time decomposition of seismic data using wavelet- based methods: Geophysics, 60, no.6, 1906- 1916.

Chopra, S., J. Castagna, and O. Portniaguine (2006), Seismic resolution and thin-bed reflectivity inversion: CSEG Recorder, 31, 19-25.

L. Goufa, Z. Hui and Z. Chao (2009), Potential risks of spectrum whitening deconvolution-compared with well driven deconvolution: Petroleum Science, v.6, pp 146-152

Haq, B. U., J. Hardenbol, and P. R. Vail, 1987, Chronology of fluctuating sea-levels since the Triassic: Science, v. 235, p. 1156-1167.

Kallweit, R. S., and L. C.Wood, 1982, The limits of resolution of zero-phase wavelets: Geophysics, 47, 1035–1046.

Mann, D.D., Eykenhof, R.H., Castagna, J.P., Ashton, C.P., 2014, Highly detailed reservoir imaging by using sparse layer inversion in a complex N.Sea turbidite: 76th EAGE Conference & Exhibition, 2014.

Marfurt, K. J., and R. L. Kirlin, 2001, Narrow-band spectral analysis and thin-bed tuning: Geophysics, v. 66, p. 1274-1283.

Matthews, S.J., Fraser, A.J., Lowe, S., Todd, S.P., Peel, F.J., 1997. Structure, stratigraphy and petroleum geology of the SE Nam Con Son Basin, offshore Vietnam. In: Fraser, A.J., Matthews, S.J., Murphy, R.W. (Eds.), Petroleum Geology of Southeast Asia. Geological Society, London, Special Publication 126, pp. 89-106.

Partyka, G., J. Gridley, and J. Lopez, 1999, Interpretational applications of spectral

decomposition in reservoir characterization: The Leading Edge, 18, 353–360.

Portniaguine, O., and J. P. Castagna, 2005, Spectral inversion: Lessons from modeling and Boonesville case study: 75th Annual International Meeting, SEG, Expanded Abstracts, 24, 1638-1641.

Pugh, Adam (2007) Structural evolution of the Nam Con Son Basin: quantitative fault analysis applied to a 3-simensional seismic dataset, Durham theses, Durham University.

Puryear, C., and J. P. Castagna, 2008, Layer-thickness determination and stratigraphic interpretation using spectral inversion: Theory and application: Geophysics, 73, R37-R48.

Puryear, C.I., Portniaguine, O.N., Cobos, C.M., Castagna, J.P. (2012), Constrained least-squares spectral analysis: Application to seismic data, *Geophysics*, Vol. 77, no. 5, p. V143-V167.

Que, P. H., 1993, Environmental and facies characteristics on the Nam Con Son Basin, *in* First International Seminar on the Stratigraphy of the Southern Continental Shelf of Vietnam, Hanoi, January 14-17, 1993, unpaginated.

Rodriguez, J.M., 2009, Spectral decomposition and inversion: case study of a production area in the Cook Inlet basin, Alaska, USA: M.S thesis, University of Houston

Sayers, J.E., 2013, Enhancement of the geological features of the Scotian basin by the application of spectral inversion, offshore Nova Scotia: M.S thesis, University of Houston

Tirado, S., 2004, Sand thickness estimation using spectral decomposition: M.S. thesis, University of Oklahoma, 63 pp.

Widess, M.B. 1973, How thin is a thin bed: Geophysics, 38(6): 1176- 1180, 1973.

Yarbrough, C. N, 2006, Pliocene to recent stratigraphy of the Cuu Long and Nam Con Son basins, offshore Vietnam: M.S thesis, Texas A&M University

Zhang, R. and J.P. Castagna, 2011, Seismic sparse-layer reflectivity inversion using basis pursuit decomposition: GEOPHYSICS, 76, NO. 6; P. R147–R158

Zhou, H.W, 2014, Practical seismic data analysis, Cambridge University Press, pp. 172-176